

**Imaging the first light:  
experimental challenges and future perspectives in the observation of  
the Cosmic Microwave Background Anisotropy**

*A. Mennella<sup>1</sup>, C. Baccigalupi<sup>2</sup>, A. Balbi<sup>3</sup>, M. Bersanelli<sup>4</sup>, C. Burigana<sup>5</sup>, C. Butler<sup>5</sup>, B. Cappellini<sup>4</sup>,  
G. De Gasperis<sup>3</sup>, F. Hansen<sup>3</sup>, D. Maino<sup>4</sup>, N. Mandolese<sup>5</sup>, M. Maris<sup>6</sup>, G. Morgante<sup>5</sup>, P. Natoli<sup>3</sup>,  
F. Pasian<sup>6</sup>, F. Perrotta<sup>2</sup>, P. Platania<sup>4</sup>, L. Valenziano<sup>5</sup>, F. Villa<sup>5</sup> and A. Zacchei<sup>6</sup>*

<sup>1</sup>INAF – IASF, Milano section, Via Bassini, 15, 20133 Milano (Italy)

<sup>2</sup>SISSA, Via Beirut 2–4, 34014 Trieste (Italy)

<sup>3</sup>Dipartimento di Fisica, Università di Roma, “Tor Vergata”, Via della Ricerca Scientifica, 1, 00133 Roma (Italy)

<sup>4</sup>Dipartimento di Fisica, Università degli studi di Milano, Via Celoria 16, 20133 Milano (Italy)

<sup>5</sup>INAF – IASF, Bologna section, Via Gobetti 101, 40129 Bologna (Italy)

<sup>6</sup>INAF – OATs, Via Tiepolo, 11, 34131 Trieste (Italy)

*Short title*

**Challenges and perspectives in the observation of CMB anisotropy**

## ABSTRACT

Measurements of the cosmic microwave background (CMB) allow high precision observation of the Last Scattering Surface at redshift  $z \sim 1100$ . After the success of the NASA satellite COBE, that in 1992 provided the first detection of the CMB anisotropy, results from many ground-based and balloon-borne experiments have showed a remarkable consistency between different results and provided quantitative estimates of fundamental cosmological properties. During 2003 the team of the NASA WMAP satellite has released the first improved full-sky maps of the CMB since COBE, leading to a deeper insight into the origin and evolution of the Universe. The ESA satellite Planck, scheduled for launch in 2007, is designed to provide the ultimate measurement of the CMB temperature anisotropy over the full sky, with an accuracy that will be limited only by astrophysical foregrounds, and robust detection of polarisation anisotropy. In this paper we review the experimental challenges in high precision CMB experiments and discuss the future perspectives opened by second and third generation space missions like WMAP and Planck.

## 1 INTRODUCTION

Quite often in the history of science major discoveries came from people who were not looking for them. This was certainly the case of the first observation of the Cosmic Microwave Background (CMB) radiation by Penzias and Wilson in 1964-65 [1]: they were lucky enough to find themselves at the right time and place, and also skilled enough to pursue to the very end the hint that Nature was offering them. But besides luck and skill two major factors were decisive in this discovery.

First, the right technology was starting to become available. Advances in millimetre-wave technology after the end of World-War II gave a boost to the young field of radio-astronomy, begun with the pioneer works of Jansky and Reber [2, 3]. The horn antenna and low noise receiver at Bell Labs was probably at the time the most sensitive microwave instrument on Earth.

Second, in the mid 60's the scientific stage was ready for this breakthrough. In 1929 Edwin Hubble's observation of the recession of galaxies revolutionised the vision of the Universe introducing the concept of "evolution" at cosmological scales [4]. About a decade before Hubble's discovery, Alexander Friedmann showed that Einstein's General Relativity equations were compatible with a variety of scenarios, both static (as developed by Einstein by introducing the "Cosmological Constant",  $\Lambda$ ) and dynamic.

In the mid 1940's, George Gamow and his group developed a physical theory of the early Universe that was compatible with both General Relativity and Hubble's observations. They extrapolated physics back in time to the point where temperature and density were sufficiently high to support nuclear fusion, and studied the production of heavy elements from primordial protons. A remarkable side-prediction of the calculations of Gamow, Halper and Hermann (see, e.g., [5]) was the presence of a photon field in the "primordial fireball", now red-shifted and cooled to very low temperatures by cosmic expansion. Penzias and Wilson, unaware of Gamow's results, observed for the first time this relic, isotropic, radiation at  $\sim 3$  K in the range

of microwaves. Their discovery was more than an experimental confirmation of a theoretical prediction: it showed that it was possible to measure directly (and precisely) properties of the Universe in a very young state, when all the processes were still in the linear regime, before structures had formed yet.

Experimental and theoretical research in cosmology has been growing steadily since then, and CMB observations have been paying a major role in this growth. In the first decade or so after the CMB discovery, major efforts were aimed at understanding the nature of the CMB radiation itself and characterising its frequency spectrum. By the early 80's the Hot Big Bang prediction of a highly isotropic background with a nearly planckian spectrum was remarkably supported by observation. The scientific community gradually became more and more interested in the study of spectral distortions and spatial anisotropies of the CMB. In particular, anisotropies were believed to be present in order to explain the existence of local non-uniformities in the present-time matter distribution.

A new phase was opened up by the COBE mission in the early 90's. The FIRAS instrument [6] measured the CMB spectrum to be planckian at the level of 99.97% in the frequency range 60-600 GHz with a temperature of  $T_0 = 2.725 \pm 0.002$  K. Coupled with sub-orbital measurements at low frequencies [7, 8, 9, 10, 11, 12] very stringent constraints to spectral distortion parameters were placed, leading to tight upper limits on energy injections in the early Universe. FIRAS demonstrated that “precision cosmology” is possible with accurate measurements of the CMB, and confirmed the maturity achieved by microwave and sub-mm technology.

A second breakthrough came from COBE with the DMR instrument which provided the first unambiguous detection of anisotropies at the level of  $\Delta T/T \approx 10^{-5}$  on large angular scales ( $\sim 7^\circ$ ) [13]. This result immediately stimulated many new experiments aiming at measuring the CMB angular distribution with increasing resolution and sensitivity. This explosion of experimental effort was motivated by the realisation that accurate measurements of the statistics of CMB anisotropies, reflected in its angular power spectrum from large scales to about  $10'$ , yield powerful constraints on fundamental parameters of cosmology such as the Hubble constant,  $H_0$ , the baryon density,  $\Omega_b$ , the dark energy density,  $\Omega_\Lambda$ , etc. To date, more than 20 independent projects have been carried out with different technologies and from a variety of ground-based and balloon-borne experiments, recently with remarkable precision.

In early 2003 the NASA space mission WMAP has released the first full-sky map of the CMB with sub-degree angular resolution, setting tight constraints on many cosmological parameters. The ESA Planck mission, to be launched in 2007, will exploit CMB temperature anisotropy measurements to its fundamental limits imposed by unavoidable cosmic variance and astrophysical foregrounds, and will likely open a new phase in CMB science aimed at a precise measurement of anisotropies in the CMB polarisation state.

Although technological advances have allowed a steady increase in the sensitivity of CMB measurements, it has also increased the level of complexity of instruments and satellites. For example, the quest for high sensitivity leads to highly sophisticated cooling systems and to multi-feed arrays, which represent new challenges for the thermal and optical design of the instruments. The combination of instrument complexity and high sensitivity leads to very severe requirements in terms of rejection of systematic effects. In the second and third generation CMB

space missions (namely WMAP and Planck) the systematic error control has become one of the most (if not *the* most) critical experimental challenge, often pushing the understanding of current technologies into poorly known grounds.

Many excellent CMB reviews have been published covering both theoretical and experimental aspects (see, e.g., [14] and references therein); however, the rapid evolutions in CMB science and in its related technologies often renew the need of state-of-the-art analysis. In this paper we present an overview of the main experimental issues of current efforts devoted to precision CMB measurements and discuss the main implications for the future challenges represented by precision polarisation anisotropy measurements. In particular the paper presents a discussion about the control of systematic effects in second and third generation space CMB experiments.

After a brief summary of the CMB theoretical background (Sect. 2) and of the main astrophysical limitations (Sect. 3) we will review the main issues concerning the control of systematic errors in high-precision CMB measurements from space, with examples taken from the (still growing) experience formed in the context of the Planck mission. Sect. 5 gives a short account of the evolution of CMB experiments from COBE to Planck, highlighting the deep relationship between progress of technology and increase in the scientific achievements as well as experimental challenges. In the last section we provide a discussion of our foreseen scenarios in CMB science after Planck.

## 2 THEORETICAL BACKGROUND

### 2.1 The hot big bang model

In the Hot Big Bang cosmological model, the expansion of the Universe started about 14 billion years ago from a state with high density and temperature ( $\rho \simeq 10^{25} \text{gr/cm}^3$ ,  $T \simeq 10^2 \text{GeV} \sim 10^{15} \text{K}$  at  $t \simeq 10^{-8} \text{s}$ ) and continues now with a progressive cooling. At primordial high temperatures matter and radiation were tightly coupled and can be regarded as a simple fluid. This holds up to  $t \simeq 3.8 \times 10^5 \text{years}$  when temperature dropped to  $T \simeq 3000 \text{K}$ : nuclei could then capture electrons to form neutral hydrogen as well as other light elements ( $^3\text{He}$ ,  $^4\text{He}$ ,  $^7\text{Li}$ ). This “recombination” process reduced the Thomson scattering cross section and photons were free to propagate and, since then, they have interacted only gravitationally with matter. These photons are the Cosmic Microwave Background and the surface surrounding us at recombination is where CMB photons have last directly interacted with matter (the Last Scattering Surface, LSS).

The Hot Big Bang model is the standard framework for cosmology since it is strongly supported by mainly three observational evidences: the abundances of the primordial light elements, the expansion of the Universe as observed by Hubble in 1926 [4] and the existence of the CMB.

Although successful the Hot Big Bang model leaves many open issues: the so-called flatness problem (i.e. why the density of the Universe is so close to the critical one), the horizon problem (i.e. why regions separated by more the  $\simeq 2^\circ$ , the angular size of causal connected regions at LSS, have the same temperature) and the origin of structures in the Universe (i.e. why the Universe is so uniform on very large scales and indeed so clumpy on smaller ones). These

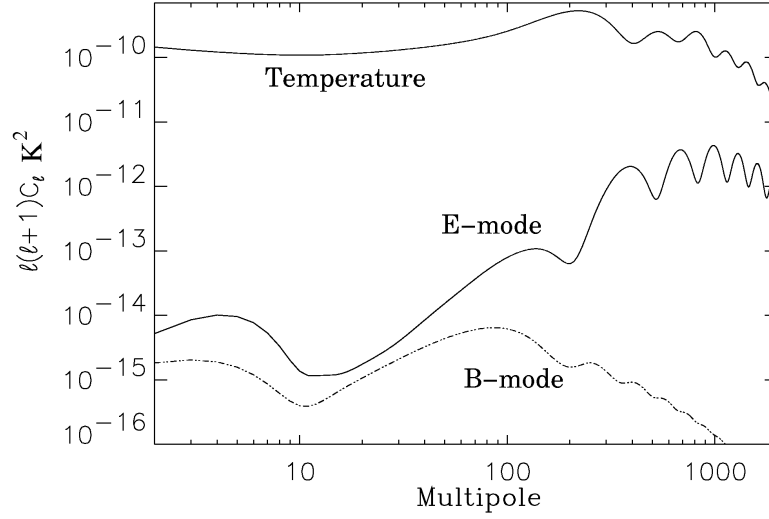


Figure 1: A typical angular power spectrum from temperature (upper curve) and polarisation  $E$  and  $B$  modes (lower solid and dashed curves).

issues are now solved by the inflationary paradigm, i.e. an exponential expansion that happened at very early times ( $t \simeq 10^{-34}$  s). A causally connected region expanded to encompass the observable Universe; furthermore quantum fluctuations present during inflation were stretched by the expansion to become, eventually, density perturbations which left their signature in the spatial distribution of the CMB. Such perturbations are predicted to have a power-law power spectrum,  $P(k) \propto k^n$ , close to scale invariant  $n = 1$ .

A common representation of the CMB field is in terms of spherical-harmonic expansion:  $\Delta T/T = \sum_{\ell m} a_{\ell m} Y_{\ell m}(\theta, \phi)$  where the multipole  $\ell \sim 180^\circ/\theta$  and the  $a_{\ell m}$  coefficients are the multipole moments which are predicted to have zero mean and variance given by  $\langle |a_{\ell m}|^2 \rangle = C_\ell$  (the angle brackets means average over all the observers in the Universe). The set of  $C_\ell$  are known as the angular power spectrum and comprise all the cosmological information if the fluctuations are Gaussian in origin (a typical example is shown in the upper curve of Fig. 1). These coefficients are the key prediction of any theoretical cosmological model. Alternative theories start from non-Gaussian primordial fluctuations and therefore their predictions could be verified looking at higher order moments in the CMB field.

The plateau at low  $\ell$  (angular scales larger than the horizon at recombination  $\simeq 2^\circ$ ) is due to the Sachs-Wolfe effect [15] i.e. the gravitational redshift and time dilation suffered by CMB photons when climbing potential wells induced by density perturbations. If the initial power spectrum is scale-invariant then  $C_\ell \propto \frac{1}{\ell(\ell+1)}$ . It is therefore usual to plot the power spectrum in terms of  $\ell(\ell+1)C_\ell$  as a function of  $\ell$  so that the Sachs-Wolfe plateau is easily recognised.

On angular scales  $0.1^\circ \lesssim \theta \lesssim 2^\circ$  causal processes in the photons-baryons fluid produce the oscillatory behaviour in the CMB power spectrum. Since recombination is nearly instantaneous, different oscillation modes were “frozen” at different oscillation phases. The first peak is due to an oscillation with a density maximum at recombination; the other peaks are harmonics of

the main oscillation. Note that between peaks velocity maxima (which are  $90^\circ$  out of phase to density maxima) prevent the power spectrum to go to zero.

Because in the short time of recombination CMB photons can diffuse a certain distance, anisotropies on scales smaller than this mean free path are erased by diffusion. This leads to the nearly exponential damping in the power spectrum (the so-called Silk damping [16]). Little contribution is expected at such scales from intrinsic CMB anisotropies.

CMB could be in principle also polarised due to Thomson scattering (which should happen in optically thin regions) between CMB photons and electrons at recombination. Furthermore it is possible to show that scattering produces net polarisation if CMB photons distribution has a quadrupole moment. This defines the main properties of CMB polarisation anisotropies which are expected (and recently detected) to be of the order of 5-10% of the temperature anisotropies (less photons contribute) and to peak at scales smaller than the horizon at recombination since the process involved is causal (see Fig 1). Any polarisation field could be decomposed into a curl-free and pure-curl components (the  $E$  and  $B$  modes). While density perturbations can produce only  $E$  modes, primordial gravity waves instead give rise to  $B$  modes, a very weak component expected to peak at large angular scales.

## 2.2 CMB and cosmological parameters

The details of the acoustic features and the overall shape of the CMB angular power spectrum depend critically on the value of several cosmological parameters such as the baryon density  $\Omega_b$ , the matter density  $\Omega_m$ , the Hubble constant  $H_0$ , the vacuum energy  $\Omega_\Lambda$  and many others, which can in principle be accurately determined by a precise measurement of the CMB power spectrum. Fig. 2 shows the dependence of  $C_\ell$  on some cosmological parameters.

- *Total Density*: decreasing  $\Omega_0$  corresponds to a decrease in the curvature with a corresponding shift of peaks toward high  $\ell$ s. In particular the position of the first peaks is  $\ell_1 \approx 200\sqrt{\Omega_0}$ .
- *Baryon Density*: increasing  $\Omega_b$  increases odd peaks (compression phase in the fluid) due to extra inertia from baryons with respect to even peaks.
- *Hubble constant*: a decrease in  $h$  ( $h \equiv H_0/100 \text{ km s}^{-1} \text{ Mpc}^{-1}$ ) with constant  $\Omega_b h^2$  means a delay in the epoch of matter-radiation equality and a different expansion rate. Peaks are boosted and slightly changed in the  $\ell$  position.
- *Cosmological constant*: increasing  $\Omega_\Lambda$  in a flat Universe, implies again a delay in matter-radiation equality with peak boosts and shifts (furthermore low  $\ell$ 's show the Integrated Sachs-Wolfe effect).
- *Spectral index*: increasing  $n$  will raise the  $C_\ell$  at large  $\ell$ 's with respect to low ones.
- *Reionisation*: if Universe is re-ionised after recombination, the power spectrum at  $\ell > 100$  would be suppressed by a factor  $e^{-2\tau}$ . Recent WMAP data suggest  $\tau \simeq 0.17$

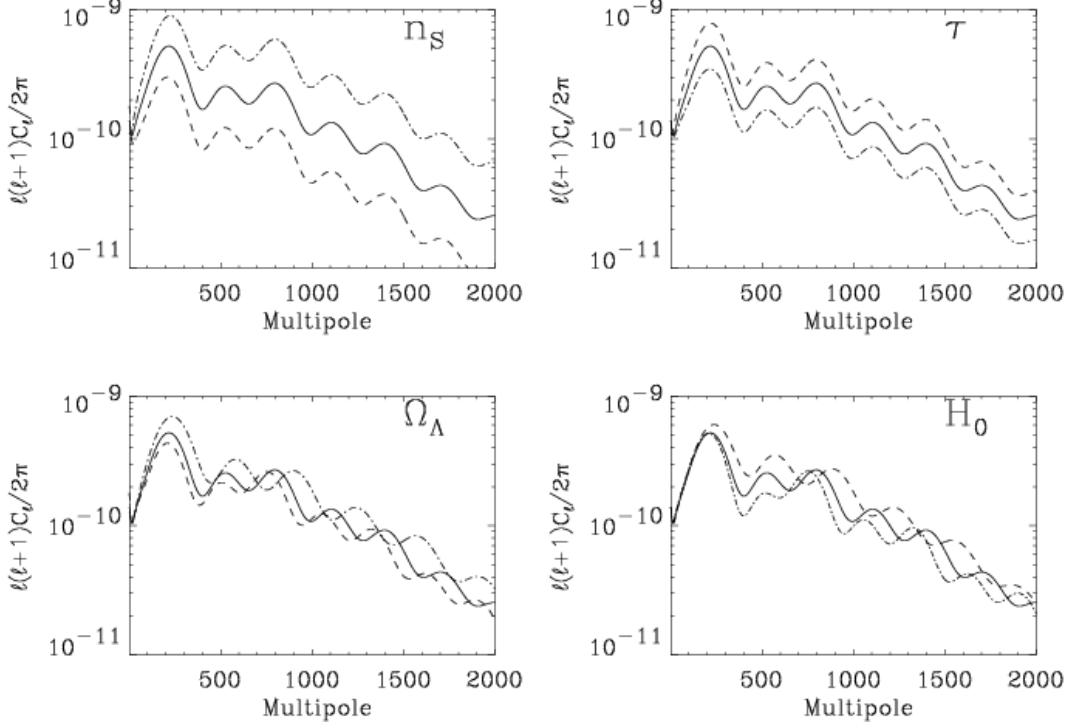


Figure 2: Examples of  $C_\ell$  dependence on some cosmological parameters

It is worth mentioning that some degeneracy between cosmological parameters do exist and different sets of cosmological parameters may produce nearly the same angular power spectrum. Some of these degeneracies (e.g. for the parameters  $n$  and  $\tau$ ) could be broken combining CMB temperature anisotropy data with polarisation data. However information from other data sets (e.g. Supernovae Type Ia data, Large Scale Structure information, HST Project) are essential in order to be combined with CMB data and provide the complete picture.

In general the best estimates of a set  $\mathbf{p} = (p_1, p_2, \dots, p_n)$  of cosmological parameters from the measured  $C_\ell$  could be obtained in a Bayesian sense by maximizing the likelihood function defined as  $\mathcal{L}(\mathbf{p}) \propto \mathcal{P}(C_\ell|\mathbf{p})\mathcal{P}(\mathbf{p}|\text{prior})$ . This is the probability of obtaining the observed  $C_\ell$  given a set of  $\mathbf{p}$  times the *prior* parameters knowledge. The actual situation is not so simple and some complications arise. One is due to the fact that the likelihood is not Gaussian in  $C_\ell$  and additional quantities have to be added for a proper likelihood characterisation [17]. Furthermore one is eventually interested in the probability distribution for a given parameter. In a Bayesian formalism the *posterior* probability of one or more parameters is obtained by marginalisation (integration) or maximisation over the other parameters. This is not a trivial task since it involves multi-dimensional integration and furthermore the overall shape of the likelihood influences the results even on a small subset of parameters.

One way to proceed is to compute the CMB power spectrum on a grid of cosmological parameters. This is time consuming since with only 6 parameters and 10 steps for each parameter,

a total number of  $10^6$  models must be evaluated. This approach is at limit for sub-orbital experiments but is probably unfeasible for space missions like WMAP and Planck. Another approach, applied to the analysis of WMAP data [18], involves Monte Carlo Markov Chains in which the parameters space is sampled randomly and results are rejected/accepted according to a precise acceptance rule. This has the advantage of scaling linearly with number of parameters allowing the inclusion of many parameters with low computational cost.

### 2.3 Secondary anisotropies

The anisotropies generated during the travel of CMB photons from the last scattering surface to the observer are generally referred to as secondary anisotropies, which can be divided into two broad classes: (i) those due to scattering of CMB photons occurring after recombination, and (ii) those arising from gravitational effects taking place along the path travelled by the photons.

One of the main causes of secondary anisotropies is hydrogen reionisation by ultraviolet light from the first stars and quasars (see, e.g., [19]). Observations of the Gunn-Peterson effect in distant quasars indicates that the Universe was completely reionised at a redshift  $z \approx 6$  [20], although little is known about the detailed ionisation history at higher redshifts. The main effect on CMB anisotropies from early reionisation is the damping of power due to the scattering of CMB photons by the free electrons [21]. The parameter governing this effect is the reionisation optical depth,  $\tau$ : peaks in the power spectrum are suppressed by roughly a factor  $e^{-2\tau}$  with respect to the low- $l$  plateau. This effect, however, is similar to the effect of a tilted spectral index in the primordial power spectrum [22], so that an accurate determination of  $\tau$  by CMB temperature observations alone is not straightforward. This degeneracy can be broken by polarisation information, since the scattering of CMB photons by the ionised medium causes the generation of large-angle polarisation anisotropy [23], providing a unique signature of reionisation. This effect has recently been used by the WMAP team to determine  $\tau$ , setting the epoch of reionisation at redshift  $z = 17 \pm 5$  [24, 25].

Reionisation of the Universe is expected to be a highly inhomogeneous process. Information on the detailed spatial distribution of the ionised medium may be obtained by studying the so-called kinetic Sunyaev-Zel'dovich effect (see, e.g., [26]), arising from the bulk motion of ionised regions, which can provide information on the size of the ionised regions and correlations between them. The magnitude of the effect, however, is very small, requiring fine angular resolution (less than  $10'$ ) and very high sensitivity ( $1 \mu\text{K}$ ) in order to be detected.

Scattering of CMB photons by hot electrons in clusters of galaxies results in the thermal Sunyaev-Zel'dovich effect [27]. Energy is transferred from the hot electrons to the CMB photons by inverse Compton scattering, leaving a distinct signature in the CMB spectrum as photons are moved from the Rayleigh-Jeans region into the Wien tail. Recently, CBI and BIMA have detected an excess of power at high multipoles ( $\ell > 2000$ ) in the CMB angular power spectrum [28] that could be explained by the cumulative effect of unresolved high-redshift clusters.

CMB photons experience gravitational redshift as they pass through regions of varying gravitational potential. This effect is known as integrated Sachs-Wolfe effect [15] and is dominant at large angular scales. This effect is strongly dependent on the dark energy content of the Uni-

verse, but is unfortunately hard to detect due to the presence of cosmic variance uncertainties at low multipoles.

Finally, when the CMB photons come across a mass concentration, their trajectories are deflected by gravitational lensing [29], causing a distortion of hot and cold spots in the CMB. For the temperature, this results in a redistribution of power and a smoothing of features in the angular power spectrum, which is increasingly important at smaller angular scales [30], while for polarisation, lensing is expected to be a spurious source of B-mode polarisation anisotropy.

## 2.4 Non Gaussianity

Standard inflationary models predict the primordial fluctuations in the gravitational potential  $\Delta\Phi$  to be nearly Gaussian distributed, which reflects in a Gaussian distribution of the CMB temperature fluctuations and of its spherical harmonic coefficients  $a_{\ell m}$ . As a Gaussian field is completely described by its mean and (co-)variances and the mean of the  $a_{\ell m}$  is zero, all the information in the CMB fluctuation field is completely contained in the variance of the  $a_{\ell m}$ , given by the power spectrum  $C_\ell$ . However, if the field is to some degree non-Gaussian, more information can be found in the higher order moments.

There are several physical effects which could introduce some small non-Gaussianities in the CMB (see, e.g., [31, 32, 33, 34, 35, 36, 37]). We will mention here three possible effects, (i) non-Gaussianities from inflation, (ii) presence of cosmic strings and (iii) a complex global topology of the Universe. The first effect comes from the fact that the fluctuations in the gravitational potential induced by inflation is a complicated function of a small Gaussian quantity  $\phi$  (related to the *inflaton* field). To second order in  $\phi$ , the gravitational perturbations can be written as

$$\Delta\Phi = \phi + f_{\text{NL}}(\phi^2 - \langle \phi^2 \rangle). \quad (1)$$

The second term in this equation introduces a small non-Gaussian part into the gravitational potential and thus into the CMB temperature field. The coefficient  $f_{\text{NL}}$  is the non-linear coupling parameter used to quantify the degree of non-Gaussianity from inflation. With  $f_{\text{NL}} = 1$ , the non-Gaussian part of the temperature field is of the order  $10^{-5} - 10^{-6}$  times the Gaussian part. In standard inflationary models  $f_{\text{NL}} \sim 10^{-1} - 10^{-2}$  [34, 37], but when we take into account evolutionary effects, it might reach a value of about 3 [38]. In more complicated inflationary models values of  $f_{\text{NL}}$  up to 100 may be possible, but even in these extreme scenarios the non-Gaussian part will be of the order  $10^{-4}$  smaller than the Gaussian part, making this kind of non-Gaussianity hard to detect.

Another kind of non-Gaussianity could arise from topological defects, which could have been created in the early Universe during phase transitions of quantum fields predicted by high energy physics. Particularly the so-called “cosmic strings” (see [39] for a review) are considered a realistic possibility. The cosmic string scenario was once competing with the inflationary theory for explaining the origin of structure in the Universe. Although recent observations of the CMB has excluded cosmic strings as the main contributor to structure formation, the possibility of a contribution from cosmic strings has not been ruled out. In this case, they would show up as small string-like discontinuities in the CMB temperature field.

Finally, another scenario which could produce non-Gaussianity signatures in the CMB is a non-trivial global topology in the Universe. In fact Einstein’s equations describe the geometry of the Universe, but leave the question of the global topology open. Some models of complex topologies would give rise not only to a non-Gaussian CMB field, but also to a non-isotropic field. In particular they predict that structures seen in one direction could be repeated in other directions on the sky (for a recent review see, e.g., [40]).

Several methods have been developed in order to detect non-Gaussianities in CMB maps. These methods can be divided into three classes: (i) pixel space methods, (ii) spherical harmonic space methods and (iii) wavelet space methods.

The most basic tests for non-Gaussianity in pixel space are tests which look at the higher order moments of the temperature field. In the simplest case, this means looking at the skewness and kurtosis of the field. The more sophisticated methods look at the higher order correlation functions, like the 3- or 4-point functions (see, e.g., [41] for a detailed description of the method). A different method to search for non-Gaussianities in pixel space is by the use of the Minkowski functionals (see, e.g., [42, 43, 44]). There are three types of Minkowski functionals, all depending on a temperature threshold,  $\nu$ . The areas in the CMB sky maps being above the level  $\nu$  are called “hot spots” and the areas below are called “cold spots”. The first Minkowski functional is just the total area of the hot spots for a given threshold  $\nu$ . The second is the contour length of all the hot spots, and the third Minkowski functional (also called the “genus”) is the number of hot spots minus the number of cold spots. For a Gaussian temperature field, the expectation value of these Minkowski functionals can be calculated analytically and compared to the Minkowski functionals of an observed sky map. Finally, one can also detect non-Gaussianity by studying the peak-to-peak correlation functions [45], the second derivative of the temperature field [46] and other geometric estimators (as in [47]).

In spherical harmonic space, the most basic methods look at the higher order moments of the spherical harmonic coefficients  $a_{\ell m}$ . In particular the bi- and tri-spectrum have been studied (e.g. [48, 49, 50, 51, 52, 53, 54]) and used to limit the non-linear coupling parameter  $f_{\text{NL}}$ . Another way to look for non-Gaussianity in harmonic space is to analyse the complex phases  $\phi_{\ell m}$  of the coefficients  $a_{\ell m}$  [55]. In a Gaussian model the phases should be uncorrelated between different  $\ell$  and  $m$  values, and non-Gaussianity could be detected by searching for correlations. Using this method one can also localise the non-Gaussianity in multipole space. Finally, one can look at the full distribution of the spherical harmonic coefficients, using the empirical process method [56, 57, 58]. By this method the distribution of the  $a_{\ell m}$  is made uniform using the cumulative distribution function, and then a Kolmogorov-Smirnov type test is used to check the degree of uniformity and independence of the coefficients distribution.

A third approach is the wavelet approach. As the wavelet transform is linear, the wavelet coefficients are expected to be Gaussian distributed in a model with Gaussian temperature fluctuations. The skewness and kurtosis of the wavelet coefficients are used to check for non-Gaussianity in CMB data [59, 60, 61, 62], and it has been shown that this is a considerably stronger test than checking the skewness of the temperature field itself.

From this summary one sees that the number of different tests to check for non-Gaussianity is large, but this is necessary as different types of non-Gaussianity tend to show up in different

tests. It is important to note that a detection of non-Gaussianity could very well be caused by incorrectly subtracted foregrounds or systematic effects in the experiment. For the COBE experiment, a non-Gaussian detection was found using the bi-spectrum [63, 64], that was later identified as a systematic effect. By applying the non-Gaussianity tests to different frequency channels maps and by applying different galactic cuts, one can determine whether a detection of non-Gaussianity is due to foreground contamination or if it could be of primordial origin.

The maps produced by WMAP have been exposed to a set of different tests of non-Gaussianity. Unresolved point sources show up as a non-Gaussian signal in CMB maps and the bi-spectrum was used to estimate the density of point sources [65]. Also, the bi-spectrum and the Minkowski functionals were used to constrain the non-linear coupling parameter  $f_{\text{NL}}$  to  $-58 < f_{\text{NL}} < 134$  at the  $2\sigma$  level [65]. Tests for phase correlations have been applied to the WMAP data and signatures of non-Gaussianity have been detected [66, 67, 68]. These non-Gaussianities have been found to be due to foreground contamination. An independent measurement of the Minkowski functionals was performed by Park [69] who reports a non-Gaussian effect in the genus statistic. Moreover the non-Gaussianity seemed to be confined to the southern galactic hemisphere. A similar asymmetry in the higher order correlation functions and the power spectra were reported by Eriksen et al [41]. Also Vielva et al [70] found that the wavelet coefficients of the southern galactic hemisphere strongly reject the Gaussian hypothesis. This asymmetry/non-Gaussianity appears to be independent of the frequency channel and galactic cut, excluding foregrounds as the cause. The source of this non-Gaussianity has not yet been found and further studies of the current WMAP maps and future CMB data sets are necessary to find its origin.

### 3 ASTROPHYSICAL LIMITATIONS

In any CMB experiment, the observed signal comprises several contributions other than the CMB itself and some are astrophysical in origin. In principle these foreground emissions can be separated from the CMB by multi-frequency observations exploiting the different spectral shapes of the signals to be separated. Due to the intrinsic smallness in the CMB signal and to the expected high sensitivity of present and future CMB experiments, the component separation process is quite delicate implying the need to disentangle the signals with few  $\mu\text{K}$  accuracy which is not trivial for both temperature and, even more, for polarisation measurements. Therefore microwave and sub-mm foreground emissions represent a challenge for CMB experiment although they provide interesting astrophysical information.

#### 3.1 Galactic Synchrotron emission

Galactic diffuse synchrotron emission arises from cosmic rays electrons accelerated in the magnetic field showing large spatial variations due to the properties of the electrons energy distributions and to the structure of the Galactic magnetic field [71]. Synchrotron radiation dominates the microwave sky emission at  $\nu \lesssim 10$  GHz. A picture of the diffuse emission at low frequency is given by the 408 MHz full sky survey [72] and two wide coverage surveys at 1420 MHz [73] and at 2326 MHz [74]. However, large sky area surveys suffer significant uncertainties related

with calibration errors, zero level and scanning strategy artifacts. Recent improvements on the analysis have minimised the systematic effects which depend on the specific experimental setup and observing strategy [75]. The synchrotron brightness temperature is a power law function of frequency,  $T_b \propto \nu^{-\beta}$ , with the spectral index  $\beta$  that varies with frequency and position, with a mean value of 2.75 at  $\nu < 10$  GHz [75]. At higher frequencies the synchrotron map evaluated from the WMAP data is now available with the synchrotron spectral index distribution between 0.408 and 23 GHz [76]. In the radio, the angular dependence of the synchrotron emission has been found to be  $\ell^{-3}$  [77] with a flatter behaviour in some selected regions of the sky [78]. Synchrotron radiation is expected to be, in principle, largely polarised (up to 70%). This could be a potential issue for CMB polarisation measurements since the CMB signal is expected at few  $\mu\text{K}$  level. Furthermore, the knowledge of polarised synchrotron emission is poor and we lack information about both frequency and spatial scalings [79, 80].

### 3.2 Galactic free-free emission

Thermal Bremsstrahlung (free-free) emission arises from hot electrons ( $T_e \gtrsim 10^4$  K) interacting with ions. The process is well known and the brightness temperature is a power law function of frequency with spectral index  $\beta_{\text{ff}} \simeq 2.15$ . However due to the flatter spectrum with respect to synchrotron radiation, free-free becomes important with respect to synchrotron only at  $\nu \gtrsim 30 - 60$  GHz where the Galactic signal is smaller than the CMB. This is why no direct templates of free-free emission are available.

Galactic free-free emission consists of two independent components: diffuse and discrete. The HII regions are the brightest discrete sources of free-free emission of our Galaxy, produced when young, massive stars (O or B type) ionise the neutral hydrogen in the interstellar medium with their ultraviolet radiation. Recently a catalog of 1442 Galactic HII regions has been produced [81] together with a study on their 3D spatial distribution [82]. The diffuse component can be well traced by  $\text{H}\alpha$  (6563 Å) emission (see the recently published full-sky  $\text{H}\alpha$  maps in [83, 84]). At large angular scales, the free free angular distribution from the available (pre-WMAP) data gives a dependence  $\propto \ell^{-3}$  [85]. By exploiting templates based on the  $\text{H}\alpha$  data, Bennett et al. [76] derived maps of the free free emission at the five frequencies observed by WMAP.

### 3.3 Galactic dust emission

Dust grains heated by interstellar radiation are responsible for Galactic dust emission in the far infrared. The total intensity depends on the chemical composition, structure and dimension of the dust grains. The frequency dependence is well modelled by a modified black-body emissivity law  $I(\nu) \propto \nu^\alpha B_\nu(T_d)$  where the brightness  $B_\nu(T_d)$  depends on the dust temperature  $T_d$  and  $\alpha \sim 2$  is the emissivity. Dust emission presents important spatial variations, as shown from the two full-sky surveys by COBE-DIRBE and IRAS. With a combination of the two surveys, a new map has been obtained [86] with the IRAS angular resolution and the DIRBE calibration accuracy. Exploiting these new data, a best fit model with two dust temperatures (16 and 9.5 K) and two emissivities (2.7 and 1.7) was proposed. From the same map, a global dust angular power

spectrum scaling  $\ell^{-3}$  has been derived. However in some high Galactic latitude regions this scaling is better represented by  $\ell^{-2.5}$  but with amplitude differing from patch to patch.

Recent analysis of COBE-DMR data [87, 88] has shown a clear correlation between DMR data at 31.5 GHz with dust emission template after the expected dust thermal emission has been removed. This “anomalous” dust correlated component is well fitted by a power law with a spectral index  $\beta \simeq 2.5$ , steeper than the expected free-free emission (although the latter is not ruled out). Further evidence of such correlation has been reported by several authors considering other data sets [85, 89, 90]. A possible explanation proposed by Draine & Lazarian [91] is the emission from spinning dust grains. However, no evidence of dust-grain emission has been found in the WMAP data.

### 3.4 Extragalactic sources

Another unavoidable limitation for CMB measurements comes from extra-galactic sources. This issue has been long discussed in the literature [92] in the context of high resolution CMB experiments, but the effect on small-scale fluctuations has not been fully understood yet. Different populations of radio and dust sources show up below and above 200 GHz. At lower frequencies the main contribution comes from radio sources (“flat”-spectrum radio-galaxies, BL Lacs objects, blazars and quasars) while at higher frequencies the main role is played by dusty galaxies. Reasonable models of source population and number counts predict that several hundreds of sources will be detected by future space missions like Planck in a wide frequency range [93].

Although relatively bright point sources can be identified and removed (by  $\sigma$ -clipping or wavelet techniques), one is left with the background of unresolved sources. Source Poisson distribution produces a simple white noise angular power spectrum with the same power at each multipole  $\ell$ . The expected level of source fluctuations is well below the CMB at frequencies between 50–200 GHz and for angular scales larger than a few arc-minutes.

In Fig. 3 we summarise the relative importance of Galactic and extra-galactic foreground fluctuations compared to the level of CMB and for different angular scales. A clear window optimal for CMB observations arises between 70–100 GHz.

### 3.5 Cosmic and Instrument related variances

“Cosmic variance” represents the ultimate accuracy limit of any possible estimation of the CMB power spectrum. The CMB field is indeed a single realisation of a stochastic process and therefore we would not expect that our observable Universe follows the average over the ensemble of possible realisation. This translates into the fact that the  $a_{\ell m}$  coefficients are Gaussian distributed random variables, at a given  $\ell$ , and therefore their variance,  $C_\ell$ , is  $\chi^2$  distributed with  $2\ell + 1$  degrees of freedom. The relative variance  $\delta C_\ell / C_\ell$  is equal to  $\sqrt{2/2\ell + 1}$  which is quite relevant at low  $\ell$ ’s due to the small number of available modes.

Beside cosmic variance, a basic limitation to power spectrum recovery concerns those experiments not probing the entire sky. Again the observed sky patch is not guaranteed to be representative of the whole sky and no direct information can be gained on scales larger than the observed patch. This variance scales with the inverse of the covered sky fraction.

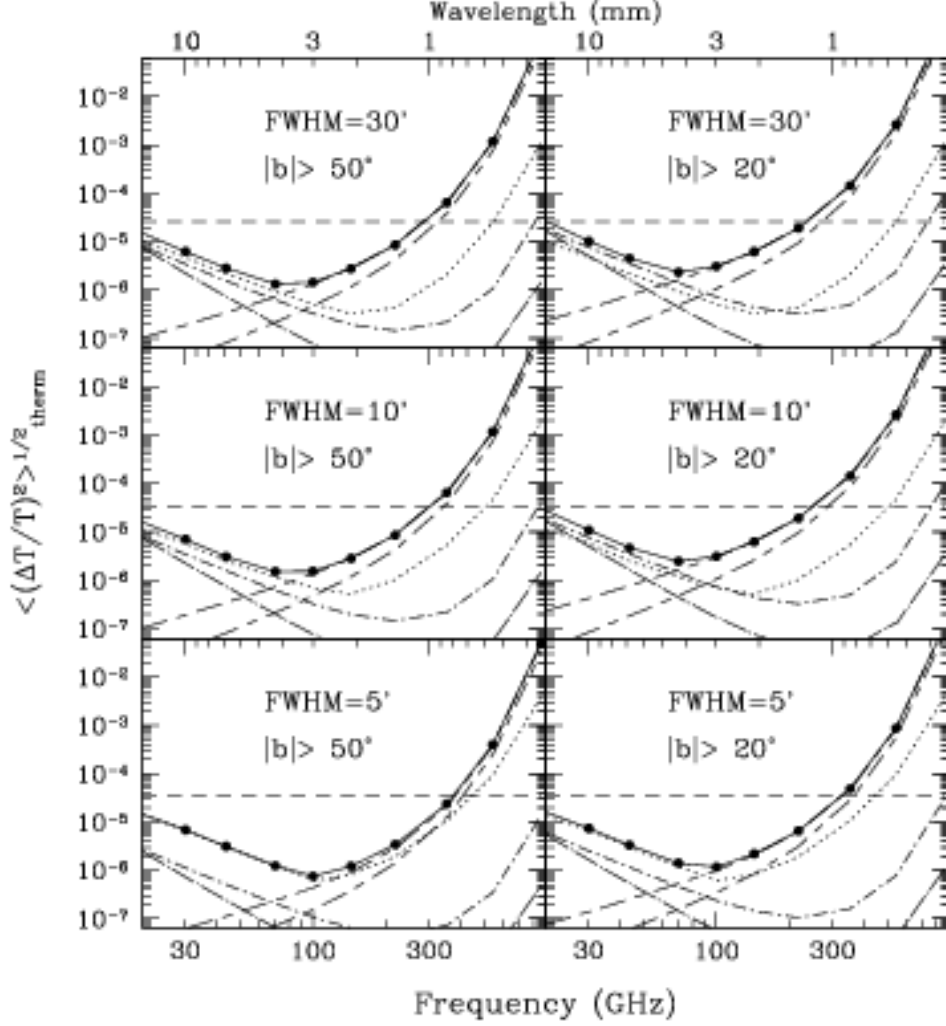


Figure 3: Temperature fluctuations for three different angular resolutions and two different cuts in galactic emission, as a function of frequency. The horizontal dashed line is the expected level of CMB fluctuations from a standard CDM model. Dot-short dashed, dot-long dashed and long-short dashed represent the mean contribution from Galactic free-free, synchrotron and dust emission respectively. Lower long/short dashed is a lower limit for Galactic dust fluctuations. The dotted curves represent the contribution from extra-galactic point sources fainter than 100 mJy [93]. The solid curve is the quadratic sum of all the contributions and the filled circles are the selected Planck frequencies (from [94]).

If we also consider instrumental noise and angular resolution, assuming perfect foreground removal, ideal calibration and no systematic effects, the relative uncertainty  $\delta C_\ell/C_\ell$  can be written as:

$$\frac{\delta C_\ell}{C_\ell} = f_{\text{sky}}^{-1/2} \sqrt{\frac{2}{2\ell+1}} \left[ 1 + \frac{A\sigma_{\text{pix}}^2}{N_{\text{pix}}C_\ell W_\ell^2} \right], \quad (2)$$

where  $f_{\text{sky}}$  is the fraction of “useful” CMB sky observed,  $A$  is the surveyed area,  $N_{\text{pix}}$  is the number of pixels and  $W_\ell$  represents the beam window function which in the case of a Gaussian beam can be represented by:

$$\begin{aligned} W_\ell^2 &= \exp[-\ell(\ell+1)\sigma_{\text{B}}^2], \\ \sigma_{\text{B}} &= \frac{\theta_{\text{FWHM}}}{\sqrt{8\ln(2)}} \frac{\pi}{60 \times 180} = (1.235 \times 10^{-4})\theta_{\text{FWHM}}, \end{aligned} \quad (3)$$

where  $\theta_{\text{FWHM}}$  represents the angular resolution in arc-minutes. In Eq. (2)  $\sigma_{\text{pix}}$  is the final noise per pixel given by  $\sigma_{\text{pix}} = \Delta T_{\text{rms}}/\sqrt{n_{\text{det}}\tau_{\text{pix}}}$ , where  $\Delta T_{\text{rms}}$  represents the rms 1-second sensitivity,  $n_{\text{det}}$  the number of detectors in the focal plane and  $\tau_{\text{pix}}$  the average pixel integration time per detector.

It is clear that the cosmic and sample variance terms dominate the uncertainty at large  $\ell$ 's while noise and beam related uncertainties dominate at higher  $\ell$ 's depending on the beam resolution and overall noise level.

### 3.6 Required accuracy for temperature and polarisation measurements

The main objective of an ideal CMB experiment is to map its temperature (and/or polarisation) anisotropy in the sky in order to accurately reconstruct the power spectrum,  $C_\ell$ , in the whole range of multipoles expected to contain information about physical processes acting at the Last Scattering Surface (i.e.  $\ell \sim 1500 - 2000$ ).

In the left panel of Fig. 4 we show values of  $\delta C_\ell/C_\ell$  (calculated by Eq. (2) for  $\ell = 1500$ ) as a function of the angular resolution and of the average noise per pixel; this figure shows that to reach relative uncertainties  $\lesssim 5\%$  at such high multipole values the instrument angular resolution and sensitivity must be within the gray area; for reference the striped box encloses the range of expected performances for the 100 GHz Planck-HFI channel. In the right panel we show two  $\delta C_\ell/C_\ell$  plots for  $\ell \leq 2000$  calculated considering the goal performance values of the W-band Planck-HFI channel and two values of  $f_{\text{sky}}$  (0.8 and 1); the figure shows that with these performances the uncertainty on the CMB power spectrum is dominated by the cosmic variance up to  $\ell \sim 1500$  even in the case in which only the 80% of the sky is available.

These requirements have profound implications on the design of an instrument aiming at reaching this kind of performances, in particular: (i) full sky coverage requires the experiment to be run from space, (ii) a  $\sim 10$  arc-minute angular resolution at 100 GHz requires the implementation of a reflector antenna with an aperture of the order of  $\sim \lambda/\theta \sim 1.5$  m, (iii)  $\mu\text{K}$  sensitivity calls for multi-feed detector arrays operating at low temperatures with long integration times ( $\gtrsim 1$  year).

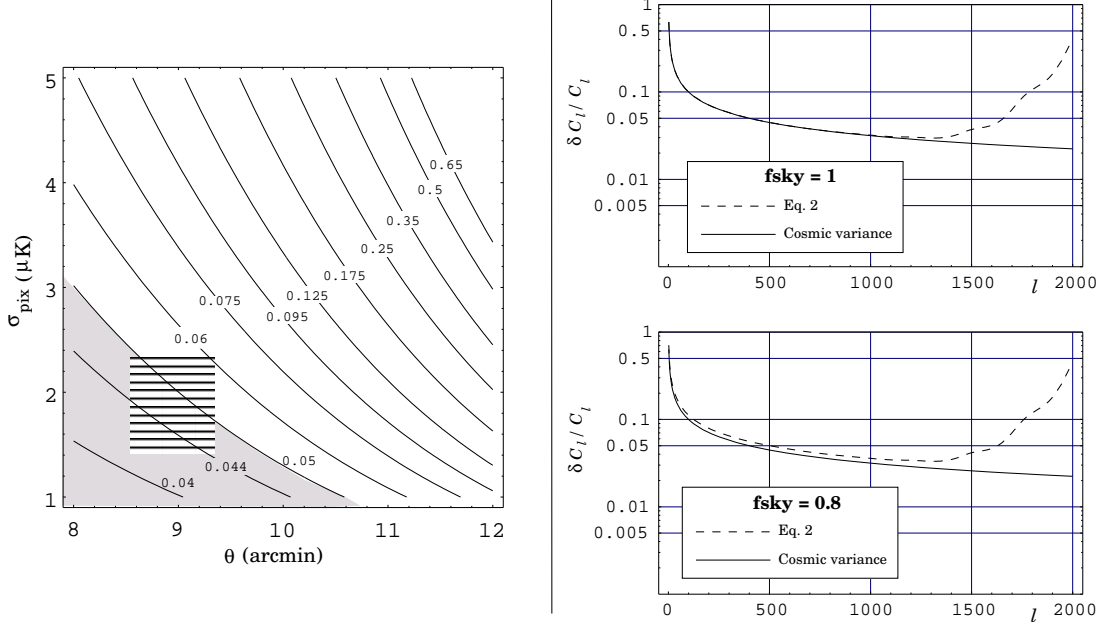


Figure 4: Left: values of  $\delta C_\ell / C_\ell$  for  $\ell = 1500$  as a function of the angular resolution,  $\theta$ , and the average noise per pixel,  $\sigma_{\text{pix}}$ . The gray area represents the range of values for  $\theta$  and  $\sigma_{\text{pix}}$  for which  $\delta C_\ell / C_\ell \leq 0.05$ ; the striped box encloses the range of sensitivity and angular resolution expected for Planck. Right:  $\delta C_\ell / C_\ell$  calculated considering the goal values of angular resolution and noise per pixel of the 100 GHz Planck-HFI channel (see Tab. 3) and two values of  $f_{\text{sky}}$  (dashed curves). The continuous curves show the contribution of the cosmic variance.

If we consider also calibration, foreground removal and control of systematic effects we need to ensure that the additional errors arising from their combination are of the order of  $\lesssim 1\text{--}2\%$  of the noise per pixel in order not to dominate the final power spectrum and image uncertainty. Calibration accuracies of the order of 1% or better can be obtained using known astrophysical sources (as the dipole for photometric calibration and bright planets for beam calibration, see Sect. 5.4.2), while accurate foreground removal is possible only with a wide frequency coverage in order to “clean” contributions from synchrotron, free-free (at frequencies  $\leq 100$  GHz) and dust (at frequencies  $\geq 100$  GHz) emissions. Similarly the level of spurious signals of instrumental and/or astrophysical signals must be at a level of  $\lesssim 2 - 3 \mu\text{K}$ , so that they do not become a dominant source of uncertainty in the final results.

For an experiment aimed at the measurement of E- and B-modes polarisation anisotropy with a comparable accuracy the instrumental requirements clearly become more stringent by 2–3 orders of magnitude (compare the levels of the temperature and the E- and B-modes polarisation power spectra in Fig. 1), which implies the availability of ultra-high sensitivity detectors and a level of scientific understanding of polarised foregrounds that is currently at the beginning. The major technological and scientific issues involved in precise polarisation anisotropy measurements can be summarised as follows:

- availability of detector arrays with sensitivity (and stability) of  $\sim 2$  order of magnitudes better compared to those adopted in temperature anisotropy measurements;
- experimental setups able to guarantee a maximum level of systematic effects at the sub- $\mu\text{K}$  level;
- templates for removing polarised foreground components with an accuracy of  $\lesssim 1 \mu\text{K}$ .

Furthermore in polarisation measurements the optical interface of the instrument needs to be more symmetrical in the response than in the case of temperature anisotropy measurements, with minimal beam distortions and sidelobes/cross-polarisation requirements that depend on the strategy assumed for polarisation measurements (e.g. X-Y differencing receivers or correlation receivers). An higher level of accuracy in optical simulations is also mandatory for systematic error control during the design phase of any polarisation sensitive instrument.

Further discussion of these issues in the context of future CMB polarisation research projects can be found in Sect. 6.

## 4 THE CONTROL OF SYSTEMATIC ERRORS IN CMB EXPERIMENTS

High sensitivity instruments provide accurate measurements of tiny signals independently from their source, so that great care must be taken to avoid experimental artifacts. The combination of increasingly sophisticated instruments and the quest for precise measurements of cosmological properties has made the control of systematic effects one of the main experimental challenges in present and future CMB experiments.

The first non trivial issue is the definition of what has to be considered a systematic effect. A unique definition, in fact, is not easy to find, as the final result of a CMB experiment depends on the combination of many factors like the characteristics of the astrophysical signal and of the optical interface (i.e. the beam shape), the instrument response, the environmental thermal and electrical stability, the data reduction algorithms.

In general we can identify three main classes of systematic effects:

1. signals in the instrument output that are not originated by the target astrophysical source (e.g. straylight effects, periodic effects caused by thermal and/or electrical fluctuations in the satellite and in the instruments, non-white components in the instrument noise spectrum);
2. effects that cause a degradation of the instrument angular resolution (e.g. beam distortions and pointing effects);
3. spurious effects generated during data processing and analysis (e.g. quantisation effects).

The second major difficulty is represented by the evaluation of the impact of a given systematic effect on the scientific output of a CMB experiment (see Sec. 4.1 for a more detailed

discussion), which is generally characterised by scientific information at three different levels: (i) temperature (or polarisation) anisotropy maps, (ii) power spectra and, ultimately, (iii) derived cosmological parameters. If the calculation of the residual effect at map level is a relatively intuitive and simple task, it is increasingly difficult to perform such an assessment at the level of power spectra and of cosmological parameters, and no standard procedures currently exist to propagate the effect of systematic errors at these levels.

The toughest challenge, however, is to set up high-precision CMB experiments that are inherently free of systematic effects. One needs to obtain *in hardware* the necessary signal stability using highly stable detectors, optimising the thermal and electrical environment and maximising the optical response in the main beam. However, when the accuracy requirements become highly demanding as in third generation space CMB experiments this ideal approach can become unrealistic because of many technical and economical constraints imposed by the development of a complex space mission. Therefore a compromise between the hardware performances and the possibility to remove *in software* the residual effects from the data is often necessary.

In the following sections we review the main categories of systematic effects with a particular attention dedicated to the experimental strategies that can be employed to reduce their impact to levels that are compatible with the scientific requirements of present and future high precision experiments.

## 4.1 Impact of systematic errors

The impact of systematic effects on the mission scientific output, is generally dependent on the level of the spurious signal at the instrument output, the pixel size and the instrument scanning strategy. A relatively simple way to perform an assessment of such impact is to simulate the measurement containing the systematic error and evaluate the residual peak-to-peak error on the generated maps.

Let us consider, for example, the periodic fluctuation in the left panel in Fig. 5 representing a spurious sky signal caused by an instrumental systematic variation (e.g. a thermal fluctuation of the telescope or a temperature variation of the radiometric receivers), which is characterised by a “slow” periodicity (i.e. with frequencies  $\lesssim 10^{-2}$  Hz) and a peak-to-peak amplitude of the order of  $\sim 1$  mK. If we simulate a measurement where the CMB signal is added to the periodic effect and then we project the time ordered data stream onto the sky we obtain the lower half of the map in Fig. 5. This particular example has been calculated assuming a strategy similar the one that will be used by the Planck satellite (see Sect. 5.4.2) i.e. a scanning in nearly great circles at the rate of 1 r.p.m. with each circle scanned  $\sim 60$  times before repointing. In the top half of the map we highlight the systematic effect signature lying about 100 times below the astrophysical signal.

Although the projection of a given periodic effect onto the sky is the most direct way to calculate the effect at map level it is also possible to estimate analytically the peak-to-peak value on the map by using a simple method that has been recently applied in the context of the Planck project to assess the impact of slow periodic systematic effects in the measured signal [95].

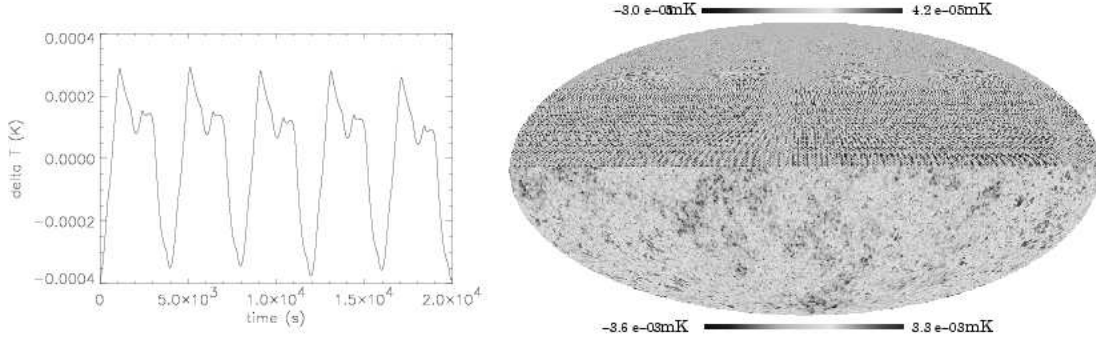


Figure 5: Simulated example of the effect of a periodic fluctuation on a CMB map. A periodic fluctuation (shown in the left panel) has been added to a simulated CMB signal; the resulting map is shown in the bottom half of the map in the right panel. The underlying systematic effect is revealed if we subtract the CMB signal (see top half of the map).

If we consider a periodic fluctuation,  $\delta T$ , of general shape in the detected signal, we can expand it in Fourier series, i.e.:  $\delta T = \sum_{j=-\infty}^{+\infty} A_j \exp(i2\pi f_j t)$ , where  $f_j$  represent the different frequency components in the fluctuation. For frequencies  $f_j$  which are not synchronous with the instrument characteristic scanning frequency,  $f_s$ , the measurement redundancy and the projection of the Time Ordered Data (TOD) onto a map with a pixel size  $\theta_{\text{pix}}$  will damp the corresponding harmonic amplitude  $A_j$  by a factor proportional to  $\sin(\pi f_j / f_s)$ . For frequencies synchronous with  $f_s$ , instead, there will be no damping and these signals will be practically indistinguishable from the sky measurement. Therefore it is critical that any spurious signal which is synchronous with the characteristic scanning frequency is carefully controlled and kept at a negligible level *in hardware*. For a spinning experiment (for example like WMAP and Planck) we can estimate the final peak-to-peak effect of a generic signal fluctuation  $\delta T$  on the map as follows:

$$\langle \delta T^{\text{P-P}} \rangle_{\text{map}} \sim 2 \left[ \frac{1}{N \times \theta_{\text{pix}} / \theta_{\text{rep}}} \left( \sum_{f_j < k f_s} \left| \frac{A_j}{\sin(\pi f_j / f_s)} \right| + \sum_{f_j < f_s, f_j \neq f_s} |A_j| \right) + \sum_{f_j = k f_s} A_j \right], \quad (4)$$

where  $\theta_{\text{pix}}$  is the pixel size,  $\theta_{\text{rep}}$  is the *repointing angle* (i.e. the angle between two consecutive scan circles in the sky),  $N$  is the number of times each sky pixel is sampled during in each scan circle and  $f_s$  represents the scan frequency. Note that Eq. (4) takes into account the damping provided only by the measurement redundancy and by the scanning strategy, without considering the possibility to detect and partially remove these spurious signals from the TOD. Several numerical strategies can be used to approach this issue and, as a general rule, the removal efficiency is greater with “slow” fluctuations, i.e. with a frequency  $f \ll f_s$ . If we denote with  $F_j$  the damping factor obtained by applying a certain algorithm to a periodic signal with frequency

$\nu_j$  then we can write Eq. (4) in the more general form:

$$\langle \delta T^{\text{p-p}} \rangle_{\text{map}} \sim 2 \left[ \frac{1}{N \times \theta_{\text{pix}}/\theta_{\text{rep}}} \left( \sum_{f_j < k f_s} \left| \frac{A_j/F_j}{\sin(\pi f_j/f_s)} \right| + \sum_{f_j < f_s, f_j \neq f_s} |A_j/F_j| \right) + \sum_{f_j = k f_s} A_j \right].$$

The evaluation of the impact of a systematic effect at the map level is generally useful for quick assessments, but for a more thorough evaluation further analysis is necessary. The next natural level is the comparison of the power spectrum of the systematic effect with the expected level of the CMB power spectrum. This allows to identify the angular regions most affected by the systematic error and provides useful guidelines to implement hardware and/or software strategies to reduce this impact if necessary.

In Fig. 6 we show the comparison between the angular power spectra of the simulated CMB map and of the periodic effect shown in Fig. 5. This example clearly demonstrates that even if a systematic effect appears to be very small in the visualisation of a map (about 100 times less than the CMB in this example) its impact on the angular power spectrum can be significant and needs to be carefully assessed.

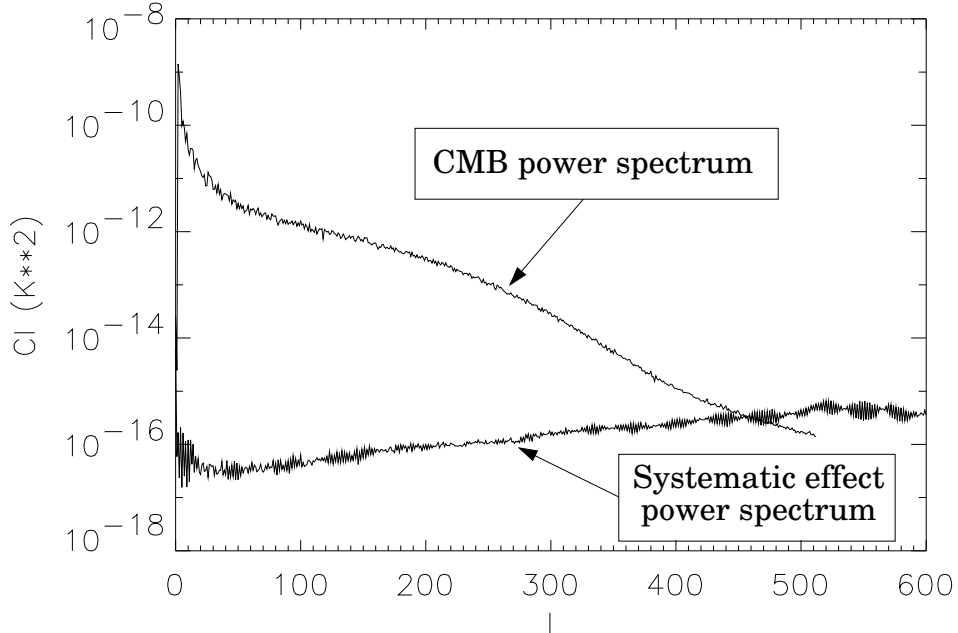


Figure 6: Simulated example of the effect of a periodic fluctuation on the CMB power spectrum.

As the ultimate goal of any CMB experiment is to calculate the most likely set of cosmological parameters from the measured power spectrum, it is of primary importance that the evaluation process of the impact of experimental artifacts is fully carried out, in order to define confidence levels that are based both on the instrument sensitivity and on the expected level of residual systematic errors. This is not a trivial task since it requires a full mission modeling for both the observation phase (instrument properties) and for the data reduction phase and therefore it

is extremely time consuming and CPU intensive. Currently there are no complete studies and standard procedures at this level; activities in this direction are in progress in the framework of the Planck Collaboration.

In the simplest approach we start from the simulation of an ideal mission with perfectly symmetric Gaussian beams and pure white noise and finally extract the cosmological parameters in this ideal case. Then for each systematic effect the same procedure is repeated and the cosmological parameters are recalculated, now with the presence of the systematic error, before and after removal in the data reduction and analysis pipeline. Of course even after the removal some residual effect (that can also be dependent on the algorithm used to clean the data) will be present which needs to be assessed.

As an example the  $1/f$  noise after correction both with destriping or map-making techniques will made noise spectrum “almost” white with a small tail at low  $\ell$ . In principle this could be a problem for the detection of the Integrated Sachs-Wolfe effects and therefore for the determination of the cosmological constant  $\Omega_\Lambda$ . However at low  $\ell$  the cosmic variance limits our knowledge of the true  $C_\ell$ . We have therefore to require residual of  $1/f$  noise to be lower than cosmic variance in order to not have an impact on cosmological parameters.

## 4.2 Optical and pointing effects

In any CMB experiment the optical system, which represents the interface between the detectors and the sky, often becomes an important source of systematic errors.

High resolution experiments generally require detector arrays coupled with a reflector antenna system, generally an off-axis telescope. Typically, the coupling between the detectors and the telescope may be realised using feeds such as corrugated horn antennas [96, 97, 98, 99] or Winston cones [100]. The angular response of the feed is modified by the telescope so that the  $(A_e \cdot \Omega_A)$  is preserved.  $A_e$  is the feed (telescope) effective aperture and  $\Omega_A = \int_{4\pi} P_n(\theta, \phi) d\Omega$  is the feed (telescope) beam solid angle, being  $P_n(\theta, \phi)$  the normalised feed (telescope) beam pattern. The greater the reflector diameter the smaller the beam solid angle and, clearly, the higher the angular resolution.

In the direction  $(\theta_0, \phi_0)$ , the antenna temperature of the telescope/feed system seeing the sky is proportional to the convolution between the brightness temperature of the sky and the normalised beam pattern:

$$T_A(\theta_0, \phi_0) = \frac{\int_{4\pi} T_b(\theta, \phi) P_n(\theta - \theta_0, \phi - \phi_0) d\Omega}{\int_{4\pi} P_n(\theta, \phi) d\Omega}. \quad (5)$$

If  $P_n(\theta, \phi)$  is not symmetric and not regular in shape, as in real cases, the observed sky will be smeared and distorted by the optics.

The effects of the main beam distortions have been extensively studied in [101, 102] for elliptical Gaussian beams and in [55, 103, 104] for complex distorted beams. Asymmetries degrade the angular resolution and increase the measurement uncertainty. In terms of anisotropy power spectrum, asymmetries will decrease the maximum achievable multipole,  $\ell$ , and will increase the error on  $C_\ell$ .

For elliptical beams, the increment in the r.m.s. temperature fluctuations due to ellipticity,  $(\delta T_{\text{rms}})_{\text{th}}$ , can be predicted easily by the following relationship [101]:

$$(\delta T_{\text{rms}})_{\text{th}} \simeq 1.11 \cdot 10^{-3} \mu\text{K} \left[ -(r-1)^2 + 2.26 \cdot (r-1) \right] \cdot \left[ -\theta_{\text{eff}}^2 + 96.0 \cdot \theta_{\text{eff}} + 1800 \right], \quad (6)$$

where  $\theta_{\text{eff}} = \sqrt{\theta_M \theta_m}$  is the “effective” Full Width Half Maximum (in arcmin) and  $r = \theta_M / \theta_m$  is the ellipticity ratio, being  $\theta_M$  and  $\theta_m$  the maximum and minimum beam angular resolutions (i.e. the major and minor axes of the elliptical 3 dB contour of the beam). For example for a beam with  $r = 1.2$  and  $\theta_{\text{eff}} = 10'$ , we obtain  $(\delta T_{\text{rms}})_{\text{th}} = 1.2 \mu\text{K}$ . In the case of complex beam shape, the amount of noise added by the distortions and the degradation of the angular resolution can be predicted performing dedicated simulations. To quantify the impact of the distortions in CMB anisotropy measurements, the effective angular resolution  $\theta_{\text{eff}}$  and the additional noise  $(\delta T_{\text{rms}})_{\text{th}}$  need to be calculated, also considering the instrument scanning strategy.

The impact of main beam distortion on the angular power spectrum is particularly relevant at the highest range of multipoles accessible to the resolution and sensitivity of a given experiment. The effect of typical scanning strategies is a beam rotation in the sky, so that the convolution (and the deconvolution) between the beam pattern and the sky signal cannot be in general performed through a simple Fourier transform. A method based on the iterative solution with the Jacobi algorithm of a linear system derived by the joint exploitation of (possibly multi-beam) time ordered data and coadded maps to recover the deconvolved sky map have been proposed by Arnau and Sáez [105]. In this framework and under quite general scanning strategy assumptions and pixelisation schemes, encouraging results have been recently found by Burigana and Sáez [106] by combining this fully blind (with respect to the sky properties) approach with Monte Carlo simulations to correct for the noise, for main beam distortion and noise levels typical of Planck.

Even if the main beam response is symmetric, the detector may collect unwanted power (straylight) that is not originated by sources in the main beam. Variations in the straylight signal cause systematic errors in measurements. Specifically, the antenna temperature can be divided into two terms:

$$\begin{aligned} T_A(\theta_0, \phi_0) &= \frac{\int_{\Omega_{\text{MB}}} T_b(\theta, \phi) P_n(\theta - \theta_0, \phi - \phi_0) d\Omega}{\int_{4\pi} P_n(\theta, \phi) d\Omega} + \frac{\int_{\Omega_{\text{SL}}} T_b(\theta, \phi) P_n(\theta - \theta_0, \phi - \phi_0) d\Omega}{\int_{4\pi} P_n(\theta, \phi) d\Omega} \\ &= T_A^{(\text{MB})}(\theta_0, \phi_0) + T_A^{(\text{SL})}(\theta_0, \phi_0), \end{aligned} \quad (7)$$

where  $\Omega_{\text{MB}}$  is the solid angle of the main beam region and  $\Omega_{\text{SL}} = 4\pi - \Omega_{\text{MB}}$  represents the solid angle of the side lobe region (i.e. the antenna response in the region outside the main beam). The signal is then picked-up by the antenna sidelobes and detected as features in the observed signal,  $T_A^{(\text{SL})}$ , that may be indistinguishable from signals induced by CMB fluctuations recorded by the main beam.

Although the real beam shape and the straylight contamination signal can be taken into account during data analysis, an optical system dedicated to high precision CMB measurements must be designed in such a way that aberrations are minimised and the straylight contamination,  $T_A^{(\text{SL})}$ , is well below the instrument final noise per pixel. Aberrations can be controlled by

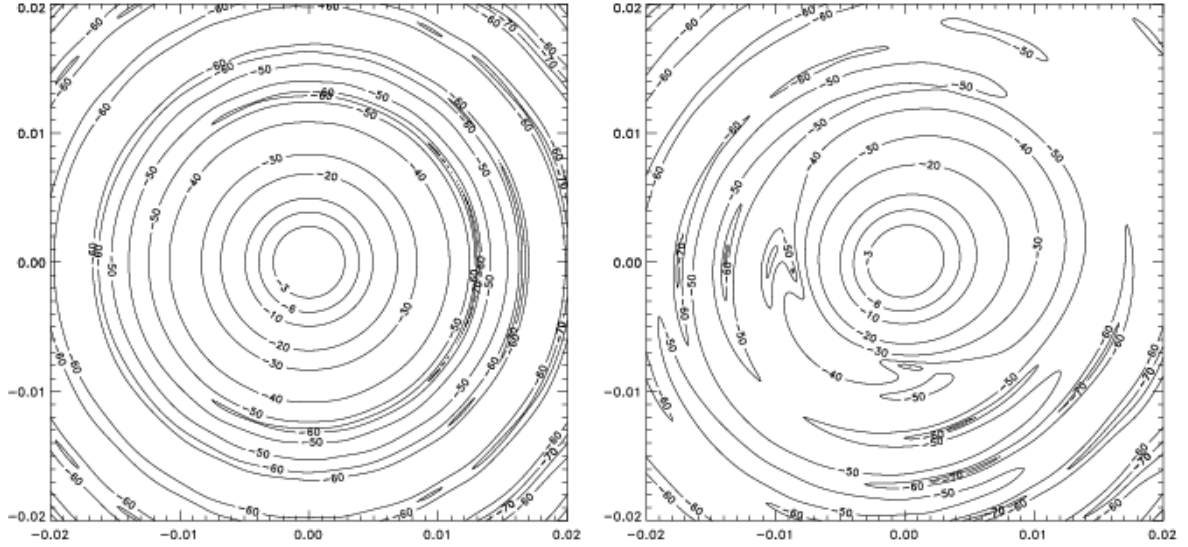


Figure 7: Left: Contour plot of a symmetric beam; typically this is the response of a detector located at the centre of the focal plane, i.e. at the nominal focus of the telescope. Right: distorted beam with mainly coma and spherical aberrations. This kind of aberration increases with the distance of the detectors from the optical axis.

implementing appropriate optical schemes in the telescope (see for instance [107, 108, 109]), while straylight can be reduced by minimizing the antenna response in the angular regions outside the main beam, or, equivalently, by minimizing the diffraction effects of the antenna system by “under-illuminating” the reflectors. This can be achieved by optimizing the design of the feeds in the focal plane (see, for example, [110, 111, 112] for the Planck case). Clearly the under-illumination has a negative impact on the angular resolution, since the telescope aperture will not be optimally used; this implies that a trade-off between angular resolution and straylight rejection is generally mandatory and this is often one of the major issues in instrument optimisation studies.

For high resolution experiments, the uncertainty in the pointing accuracy may be another serious source of degradation. A typical requirement is that the pointing error,  $\sigma_p$ , should be a small fraction of beam angular resolution. Typically  $\sigma_p \leq 0.1 \cdot \theta_{\text{eff}}$ . The uncertainty in pointing direction and its knowledge has a direct impact on the effective angular resolution and this translates into a restriction of the multipole range effectively probed. In fact, the “real” beam shape is determined by the convolution of the beam with the statistical distribution of the pointing uncertainty and this affects the sky angular power spectrum at high multipoles. Usually, the shape of the main beams will be reconstructed during the observation phase by means of bright point sources such as planets or supernova remnants. The accuracy of beam reconstruction is strongly dependent on the pointing accuracy, being the pointing accuracy a limiting factor for the proper knowledge of beam resolution and shape. This leads to an additional uncertainty in the evaluation and subtraction of the systematic effects introduced by

main beam distortions in the angular power spectrum at different multipoles.

It is worth mentioning that pointing reconstruction and, therefore, beam reconstruction, can be obtained only with the combination of scientific data (e.g. data from bright point sources like Jupiter) together with attitude data. These include CCD-camera, star-mapper or star-tracker systems to map the sky for bright known stars which would eventually yield the attitude reconstruction. From attitude it is possible to derive pointing information for each feed in the focal plane. The process is usually iterative where improved solutions for both pointing and beam shape are progressively up-dated until the final accuracy is achieved.

### 4.3 $1/f$ noise and thermal effects

Detector noise is generally represented by a spectral density [113] characterised by the following features: a wide, flat plateau at high frequencies (white noise plateau), a steep rise at low frequency ( $1/f^\alpha$  region), some lines at particular frequencies, which are generally caused by periodic fluctuations in the thermal and/or electrical environment (see Fig. 8).

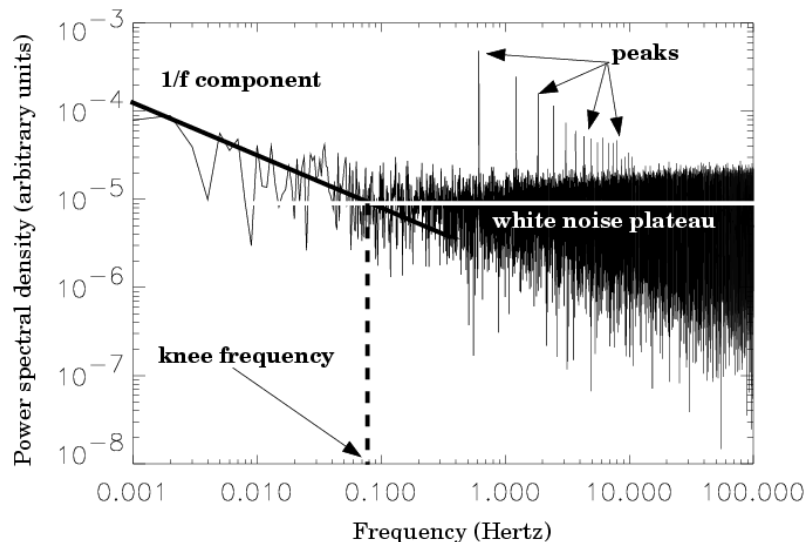


Figure 8: Typical noise power spectrum showing the white noise plateau, a  $1/f$  component at low frequencies and periodic peaks.

Let us now examine the main causes of instrumental noise: Johnson (thermal) noise, temperature noise, shot noise,  $1/f$  noise, photon noise.

Voltage fluctuations across a resistor, a linear function of its physical temperature, are the cause of the so-called Johnson noise [114, 115], caused by random motion of carriers in a conductor, which results in a fluctuating voltage across the terminals,  $\delta v_f$ . Its power spectrum is white [116] and given by:

$$\langle \delta v_f^2 \rangle df = S_V(f) df = 4 k T R df, \quad (8)$$

where  $k$  is the Boltzmann constant,  $T$  is the physical temperature,  $R$  is the element resistance.

Shot noise (sometimes called “Schottky noise” [117]) occurs when a phenomenon may be described as a series of independent events occurring randomly. For instance, crossing of a p-n junction by electrical carriers in a transistor produces a current,  $\delta i_f$ , which is affected by shot noise. This kind of noise, which does not depend on the physical temperature, is observed in semiconductor devices. Also in this case the power spectrum is white. The following formula illustrates the case of a transistor [113].

$$\langle \delta i_f^2 \rangle df = S_I(f) df = 2eI df, \quad (9)$$

where  $e$  is the electric charge,  $I$  is the current. Generation-recombination noise, due to the random fluctuating rates of generation and recombination of free carriers in semiconductor devices, may be considered a form of shot noise. However, since it modulates the current passing through the device by changing its impedance, it is usually treated in a separate way.

Flicker noise is characterised by a  $1/f^\alpha$  (where  $\alpha \approx 1$ ) behaviour in the power spectrum below the so-called “knee frequency”, which is the frequency at which the power of the  $1/f$  component equals the white noise plateau (see Fig. 8). It can be produced by many different sources [118], and in some cases it is due to generation-recombinations noise modulated by other effects. It also arises in semiconductor/metal junctions, but its origin remains partly unknown. This type of noise represents one of the major issues in the development of HEMT-based (HEMT = High Electron Mobility Transistor) radiometric receivers for CMB observations. Its effect can be minimised by means of differential measurements strategies in which the sky signal is compared to a signal received from another point in the sky (as in COBE and WMAP [119, 120]) or from a stable internal cryogenic reference load (as in Planck-LFI [95, 121]).

A fundamental noise is the photon noise, due to the statistics in the arrival time of photons and resulting in a fluctuating detected power. This kind of noise is strongly dependent on the temperature: thermal emission from telescope mirrors (which are gray bodies with few percent emissivity  $\epsilon$ ) in a room temperature environment, for example, may be a concern for sensitive observations. It can be shown that the power fluctuation spectrum is:

$$\sqrt{\langle (\Delta W)^2 \rangle} df = \text{const.} \times T^{\frac{5}{2}} f(\epsilon), \quad (10)$$

where the constant depends on the particular experimental setup, while  $f(\epsilon)$  is zero when  $\epsilon = 0$ . In space telescopes, which may be passively cooled to 50 K or below, this effect is strongly reduced.

As a general rule, as it is evident from the noise spectral densities, a general benefit is obtained by cooling detectors and optics at the lowest possible temperature. This is obtained by using cryogenic detectors (radiometers between 20 K and 4 K, bolometers between 300 mK and 100 mK) and cold optics (for instance, a passively cooled telescope in space may reach 35 K). However, this is not sufficient to reach the stability required in CMB observations. Temperature in all the detection sub-systems must be not only low but also stable.

The response of receiver components generally depends on their temperature, so that a variation in physical temperature necessarily induce a variation in the receiver output. If temperature

fluctuations are random then the effect is an increase in the receiver white noise level; if, on the other hand peculiar frequency components are present then the effect is a systematic variation of the final measurement.

For example, in differential radio receivers, any fluctuation which impacts asymmetrically on the two receiver legs upstream of the differential element (e.g. a variation in the reference signal or a fluctuation in the telescope temperature) will mimic a “true” sky signal; similarly bolometric detectors must be operated with constant power background. If any element between the sky and the detector (e.g. a bandpass filter) is characterised by a non-ideal transmission then any temperature fluctuation will mimic a “true” signal on the detectors.

It is therefore mandatory to reduce temperature fluctuations of the receiving system to the lowest possible values, taking into account several aspects in the instrument design, like shielding receivers from external sources, minimising internal temperature fluctuations, providing a stable reference signal.

Thermal fluctuations from the external environment are generally minimised by placing shields around the focal plane and by designing orbits and scanning strategies that provide a thermal environment as stable as possible (e.g. see the examples of WMAP in Sect. 5.3 and Planck in Sect. 5.4).

Stabilisation of the intrinsic payload and instrument temperature is generally obtained by a combination of passive (with low thermal conductivity and high thermal capacity materials like carbon fiber) and active (with PID<sup>1</sup> control loops) strategies.

Trade-offs must often be reached between instrument feasibility (in terms of technology and costs) and control of systematic effects. A careful study of the receiving system can also lead to split requirements between different perturbing components, in order to control systematic effects at the maximum possible level.

## 4.4 Effects from data handling

### 4.4.1 Signal quantisation and telemetry losses

In space CMB experiments the analog instrument output is digitised and stored during the acquisition in an on-board buffer memory which is periodically downloaded to ground. Data are usually sent as a sequence of packets containing the relevant data and ancillary information (time, voltages, temperature sensors) that allows the on-ground reconstruction of the data stream. Depending on their content, packets are usually defined “scientific” packets, carrying measured data, and “house-keeping” packets, containing sensor data, alarms and telecommands<sup>2</sup>.

The effective amount of scientific data which may be recovered by the receiving station during an observation is

$$I_{\text{eff}} = C_r(1 - f_{\text{hk}} - f_{\text{cnt}}) \left[ \frac{B_{\text{ch}}}{1\text{bit/sec}} \right] \left[ \frac{T_c}{1\text{sec}} \right], \quad (11)$$

---

<sup>1</sup>PID = Proportional Integral Derivative

<sup>2</sup>See ECSS-E-70-41A standard ([www.ecss.nl](http://www.ecss.nl)) for packets definitions and use in space missions

where  $B_{\text{ch}}$  represent the communication bandwidth,  $T_c$  the connection time,  $f_{\text{cnt}}$  and  $f_{\text{hk}}$  the fraction of telemetry allocated for contingencies.

The term  $C_r$  represents a compression factor applied to scientific data before telemetry in order to optimise the available bandwidth and which is usually obtained through a combination of lossy (data quantisation) and lossless (arithmetic compression algorithms) strategies.

Lossy compression schemes clearly can introduce additional noises and systematic effects into the scientific data stream. For CMB data acquired by a stable instrument, and for short times, data are roughly normal distributed, and the distribution is dominated by the instrumental white noise, plus minor contributions from the CMB dipole, the Galaxy and point sources. In these conditions the loss-less compression factor  $C_r^{\text{lossless}} < N_{\text{bits}}/\log_2(\sqrt{2\pi e}\sigma/q)$  being  $\sigma$  the data RMS,  $q$  the digitisation step and  $N_{\text{bits}}$  the number of bits used by the on-board electronics (see [122] and references therein). This relationship shows that this factor increases by decreasing the value of  $\sigma/q$  which can be optimised by adding a re-digitisation step on the on-board processing before compression.

The impact of digitisation in CMB experiments has been studied in detail (see [123] and references therein). The main result is that digitisation adds a constant baseline to the derived CMB power spectrum, which can be estimated and removed once  $q$  and the scanning strategy are known. Digitisation also introduces spurious noise into time ordered data and maps which may possibly affect CMB non-Gaussianity studies.

Packet loss or corruption (generally of the order of  $\sim 5\%$ ) may cause errors in the data reduction with the consequent introduction of additive noises and systematic effects (see [124] for a review of the various causes that may induce telemetry loss). This effects are generally reduced by requiring the maximum degree of independence (at the cost of some redundancy loss) among packets, so that the interpretation of the content of each packet can be done independently from the other packets<sup>3</sup>.

Random loss of scientific packets acts as a source of noise with a limited impact, if re-observation of the same region of sky in different periods is possible. In particular it has been demonstrated [124] that under general conditions a higher observation redundancy with higher telemetry losses is favourable with respect to a lower redundancy with lower telemetry losses. The strongest impact from this effect is in the study of foregrounds, which is dependent on the local details of the signal distribution in the sky rather than on the full sky statistics.

Telemetry losses of large portions of scientific or housekeeping data may cause effects which are not easy to predict. An example is the loss of a packet which carries the confirmation of execution of a telecommand which changed an instrumental parameter; in this case it may be non trivial to understand on ground from which sample in the data stream the parameter change has to be applied by the data reduction pipeline. Depending on the level of telemetry redundancy, this uncertainty may affect one or tens of packets. The effect is particularly important if more parameters are changed in turn. Packets independence may allow to mitigate it.

---

<sup>3</sup>Packets independence is often required also because in some circumstances they may be sent randomly in time to the receiving station

#### 4.4.2 Map making

Optimal algorithms for producing maps from time ordered data are a primary task in CMB data analysis. The large data sets involved, the low signal-to-noise per sample and the complex correlation structure require computationally challenging and advanced statistical methods to solve the problem. Furthermore, map making can also be used to flag and cure systematic effects in the time ordered data which may have negative impacts on the scientific analysis.

A special kind of systematic errors are those produced during data analysis itself. Although not immune by data handling errors, as explained below, state of the art map making codes produce very modest artifacts. Making maps out CMB experiment timelines allows for a lossless compression of the raw data with minimal assumptions.

Map-making *a la COBE* (see, e.g., [125]) has been extended to the differential, high resolution WMAP experiment [76, 126]. In experiments like COBE and WMAP (in which the difference is taken between two essentially equal sky signals) the noise is nearly white [127], so that the map making problem reduces in this case to reconstructing the field from a set of differences. A more complicated problem arises in the case of differential measurements where the difference is taken between two slightly different signals (such as in Planck-LFI) which are characterised by a somewhat simpler experimental structure but contamination by  $1/f$  noise (see, e.g., [126, 128] and Sect. 5.4.2) needs to be taken into account.

The instrument measurement can be modelled as the re-projection over time of sky observations (the scan), plus a contribution from noise. In doing so, we assume that the data,  $\mathbf{d}$ , depend linearly on the map,  $\mathbf{m}$ <sup>4</sup>:

$$\mathbf{d} = \mathbf{P}\mathbf{m} + \mathbf{n}, \quad (12)$$

where  $\mathbf{n}$  is a vector of random noise with (in general) non diagonal covariance. The rectangular,  $\mathcal{N}_d \times \mathcal{N}_p$  matrix  $\mathbf{P}$  is called *pointing matrix* and models the scan by “unrolling” the map over the timeline. Because of efficiency considerations, it is normally assumed that beam smearing effects are taken into account at the map level, i.e. hidden in  $\mathbf{m}$ . This is meaningful only if the beam profile is symmetrical. In this case, the structure of  $\mathbf{P}$  for a one-horned experiment would then be very simple. Only one element per row would be different from zero, the one connecting the observation of  $j$ -th pixel to the  $i$ -th element of the time stream.

Many methods have been proposed to estimate  $\mathbf{m}$  in Eq. (12) (for a review see, e.g., [128]). Since the problem is linear in  $\mathbf{m}$ , the use of a Generalised Least Squares (GLS) method appears well suited. This leads to a solution of the form:

$$\tilde{\mathbf{m}} = \Sigma^{-1} \mathbf{P}^T \mathbf{N}^{-1} \mathbf{d}, \quad (13)$$

where

$$\Sigma = \mathbf{P}^T \mathbf{N}^{-1} \mathbf{P}. \quad (14)$$

In the above equations  $\mathbf{N}$  is the noise covariance matrix, that must be estimated from the data themselves.

---

<sup>4</sup>For the sake of simplicity, we restrict to the case of temperature-only measurements. For an instrument with linear polarisation capabilities, a very similar formalism can be written to account for the Stokes linear polarisation parameters.

Although optimal in a statistical sense (if the noise is Gaussian Eq. (13) is a Maximum Likelihood solution), the method outlined above is computationally unfeasible for large datasets, because of the size of the matrices involved (of order  $10^5$  to  $10^7$ ). The solution is to keep the same equations, recasting them into a different manner to allow for the use of an iterative solver. The latter is much less computationally demanding than ordinary linear algebra techniques, because it only requires matrix to vector products. The map making problem is naturally suited for such a scheme. In fact, application of the matrix  $\Sigma$  to a vector can be thought as the “unrolling” of a tentative solution map over the timeline (application of  $P$ ), the subsequent application of  $N^{-1}$  (a convolution if the noise is stationary) and, finally, the application of  $P^T$  which sums back the convolved data into a map. This approach, usually named “unroll, convolve and bin” [129, 130] can be successfully embedded into an iterative scheme (usually relying on a conjugate gradient solver) to converge efficiently to the required solution.

The “unroll, convolve and bin” approach has solved the problem of producing maps for large datasets, a problem deemed unfeasible until a few years ago. Moreover, its computational efficiency has allowed this method to be inserted into a Monte Carlo chain, thus providing a powerful tool to check the robustness of a data analysis pipeline and flag sources of errors. In particular, it has been shown that in most applications the map making stage itself introduces little, and usually negligible, artifacts in the data.

In this respect, the potentially more dangerous source of error is to be located in the way the beam is handled. The scheme outline above assumes symmetric beams and is prone to inject systematic errors should this assumption fail. Removing this limitation, which is more a limitation of the data model rather than of the map making scheme itself, is at the present time the frontier in this area of CMB data analysis.

#### 4.4.3 Destriping

In the previous section we have addressed the issue of correlated  $1/f$  noise in the production of optimal maps. When coupled to the observing strategy,  $1/f$  noise will generally produce “stripes” in the final maps. Besides map-making there are other approaches that can deal with  $1/f$  noise striping as well as with a large variety of systematic effects, usually called “destriping” [131].

These algorithms do not solve for the map but eventually obtain time ordered data cleaned from the low frequency systematic effect. They can be then used for many applications: in-flight main beam reconstruction [132, 133] and calibration [134], studies of (and cleaning from) radio-source variability [133] and Solar System objects, map production from cleaned time ordered data. Although destriping does not guarantee that the final map will be the minimum variance map, in terms of final noise power spectrum, the two approaches are virtually identical. In addition, accurate numerical simulations [135, 136] have shown that the quality of destriping results, both in terms of de-drifting of time ordered data and of map and power spectrum recovery, is largely unaffected by the presence of optical distortions (both in the main beam and in the sidelobes), as the differences between the measurements at the same crossing points are largely dominated by the noise.

It is however worth mentioning the approximations for which the destriping approach is valid. Destriping assumes that the overall effect of  $1/f$  noise can be approximated by an additive constant. This condition is verified as long as the natural spinning/observing frequency is large compared to the  $1/f$  noise knee-frequency (see, Sect. 4.3), which in the case of Planck-LFI this implies to work with averaged (over 1 hour period) scan circles, while for the HFI instrument (which shows lower knee-frequencies) it is possible to work directly with elementary (1 minute) rings.

If we assume that the  $1/f$  noise effect is well approximated by a single baseline for each scan circle  $A_i$ , it is possible to recover the baselines which are obtained using all the possible crossing points between different scan trajectories. Formally this means to solve the linear system:

$$\sum_{\pi=1}^{n_c} \left[ \frac{[(A_i - A_j) - (T_{i\ell} - T_{jm})][\delta_{ik} - \delta_{jk}]}{E_{ij}^2 - E_{jm}^2} \right]_{\pi} = 0, \quad (15)$$

for all the circles  $k = 1, \dots, n_s$ . Here  $\delta$  is the usual Kronecker symbol,  $A_i$  are the baselines to be recovered,  $T_{jl}$  is the observed signal in the ring  $j$  at the position  $l$  along the ring. The terms in the denominator are the level of white noise for the same pixel. This system simply translated into:

$$\sum_{h=1}^{n_s} C_{kh} A_h = B_k, \quad k = 1, \dots, n_s, \quad (16)$$

which can be easily solved. The matrix of the coefficients  $C_{hk}$  is in general positive defined, symmetric and non singular provided that there are enough intersections between different scan circles.

## 5 CMB EXPERIMENTS

In this section we review briefly the evolution of CMB anisotropy experiments from COBE to WMAP and describe the next planned mission of the European Space Agency, Planck. A more detailed and complete review of experiments before WMAP can be found in [14].

### 5.1 From COBE to WMAP

The first detection of anisotropies was achieved by COBE-DMR with three pairs of Dicke-switched radiometers at 31.5, 53 and 90 GHz. As in any CMB experiment, the success of DMR depended on the accurate control of systematic effects and calibration [137]. The DMR 4-year frequency-averaged map has a signal-to-noise ratio of  $\sim 2$  and gives a visual impression of the actual large scale CMB structure in the sky. The observed power spectrum, limited to  $\ell < 20$ , was found to be consistent with a scale-invariant spectral index ( $n_s \sim 1$ ) of the primordial density fluctuations [138], and a power-law fit yielded an extrapolated quadrupole term of  $15.3 \mu\text{K}$  [139]. The DMR results proved the presence of temperature fluctuations at a measurable level  $\Delta T/T_0 \sim 10^{-5}$ , and started the race to unveil new features in the angular power spectrum. Increasingly ambitious sub-orbital programs were carried out mostly aiming at sub-degree scale detections in limited sky regions.

### 5.1.1 Ground-Based Experiments

High altitude, dry sites have provided excellent results, in spite of the limitations of atmosphere and ground emissions. With only a few exceptions [140], most ground based experiments take advantage of the atmospheric windows below 15 GHz, around 35 GHz and 90 GHz. The Tenerife experiment, carried out from the Teide site (2400 m) used similar technology as DMR in the 10–33 GHz range [141]. Soon after COBE, it was possible to detect CMB anisotropy at a level  $\sim 40 \mu\text{K}$  in the multipole range  $\ell \sim 10\text{--}30$ , overlapping with DMR. More recently, a 33 GHz interferometer was installed [142] at Teide scanning a sky portion largely overlapping the original program. The detection of CMB anisotropy was unambiguous, with  $\Delta T_\ell \sim 43 \mu\text{K}$  at  $\ell \sim 110$ .

Even if harsh and isolated, such as the Antarctic Plateau, ground based sites offer the enormous advantage of reachable instruments and long integration times. The UCSB degree-scale measurements from the Amundsen-Scott South Pole Station carried out in the period 1988–1994 with HEMT cryo receivers at 30–40 GHz [143] showed correlated structure with amplitude  $\Delta T_\ell \sim 33 \mu\text{K}$  at  $\ell \sim 60$ . The polar site also hosted the Python/Viper program, leading to detection at  $\sim 1^\circ$  scales using an off-axis parabolic telescope that was coupled either to bolometers at 90 GHz [144] or to a HEMT radiometer at 40 GHz [145]. The results were consistent with DMR at low  $\ell$ 's, and suggested an increase at  $\ell > 40$ . Viper was a follow up of Python at higher angular resolution [146] with observations at 40 GHz with a large 2.15 m telescope, yielding sensitivity in the range  $100 < \ell < 600$ .

The Saskatoon instrument [147] used an off-axis parabolic reflector and total power receivers based on low-noise cryogenic HEMT amplifiers, and produced one of the first convincing evidences of a raising spectrum (from  $\Delta T_\ell \sim 49 \mu\text{K}$  at  $\ell \sim 87$  to  $\Delta T_\ell \sim 85 \mu\text{K}$  at  $\ell \sim 237$ ). As a follow-up, the MAT program probed smaller scales,  $40 < \ell < 600$ . The Saskatoon instrument was installed at a site near Cerro Toco (5240 m) with the addition of a 144 GHz channel (0.2 beam), taking advantage of both HEMT and SIS technologies. The MAT/TOCO 31 and 42 GHz instruments were flown twice in 1996 (QMAP) to perform degree-scale observations providing detection in both flights [148].

At small angular scales, a series of filled-aperture observations at OVRO lead in the late 90's to an unambiguous detection [149] in the range  $7'$  to  $22'$ . Interferometers have provided high-quality observations at high  $\ell$ 's. The CAT three-element array operating at 13–17 GHz showed detection at  $\ell \sim 420$  [150]. The VLA has been used to set limits to CMB anisotropy at sub-arcminute angular resolution since the early 80's and established new upper limits in the range  $0.2'$  to  $1.3'$  [151]. ATCA [152] yielded upper limits in polarised intensity and  $\Delta T_\ell < 25 \mu\text{K}$  for multipoles  $3300 < \ell < 6000$ . Finally, the SuZIE bolometer array [153] operated at Mauna Kea gave upper limits to CMB primary anisotropy. The combination of all data at high resolution gives evidence for a downturn in the power spectrum at sub-degree scales, as expected by standard models.

Three high quality ground-based data sets have been recently obtained. The DASI 13-element interferometer [154] used cryogenic HEMTs in the 26–36 GHz spectral window and observed from the South Pole in the 2000 austral winter. The results mapped the power spectrum in the range  $100 < \ell < 900$ . The first peak at  $\ell \sim 200$  was evident and in good agreement with

results from other experiments. In addition, the DASI data suggested the presence of further peaks at  $\ell \sim 550$  and  $\ell \sim 800$ . DASI was also sensitive to polarisation anisotropy and produced maximum likelihood EE, BB, and TE power spectra, probing interesting upper limits on EE and BB modes for some multipole ranges and showing also interesting detections in a quite good agreement with theoretical estimations [155]. The CBI interferometer was sensitive to scales from  $5'$  to  $1^\circ$  ( $300 < \ell < 3000$ ). Excellent observations were obtained [156] with power spectrum results in good agreement with other experiments at  $\ell < 2000$  but extending up to  $\ell \sim 3000$ . An excess power was observed at high  $\ell$ 's suggesting a Sunyaev-Zel'dovich effect. Even more recently, the Viper 2.1 m telescope was used at the South Pole in the ACBAR experiment [157] to obtain two deep fields of the CMB, 3 degrees in size, with an rms of  $8 \mu\text{K}$  per  $5'$  beam.

## 5.2 Balloon-Borne Experiments

Although the reduction of atmospheric emission from balloon altitudes (35–40 km) is great (factor  $\sim 10^3$ ), in conventional flights the available observing time is only about 10–12 hours. In recent years, long-duration balloon (LDB) flights (10–15 days) have been successfully flown. Early balloon experiments confirmed the DMR detection. The FIRS bolometers covered about  $1/4$  of the sky at  $\sim 3.8^\circ$  resolution [158] in the range 170–680 GHz. The ARGO degree-scale bolometric experiment [159] lead to a detection of CMB anisotropy  $\Delta T_\ell \sim 39 \mu\text{K}$ . BAM obtained statistically significant detection at degree scales ( $\Delta T_\ell \sim 56 \mu\text{K}$  at  $\ell \sim 75$ ) [160] using a cryogenic differential Fourier transform spectrometer coupled to a 1.65 meter reflector. The MAX and MSAM balloon-borne multi-band bolometric receivers contributed to the progress at sub-degree scale. MAX was flown 5 times between 1989 and 1994 and observed in nine different sky regions yielding seven positive anisotropy detections [161]. The results also suggested a band power at degree-scales higher than DMR. MSAM [6] observed a  $10^\circ$  region with  $30'$  resolution. MSAM was launched 3 times in the period 1992–95, each flight detected a clear CMB anisotropy signature. A combination of the three flights yielded data points in three power bands centred at  $\ell \sim 34, 101, 407$ .

Boomerang and Maxima represented a major breakthrough. Boomerang was launched for its first LDB flight around Antarctica in December 1998 and landed roughly 10.5 days later. An array of bolometric detectors at 90, 150, 240 and 410 GHz were cooled by a  $^3\text{He}$  refrigerator to 0.28 K. The first results [162] were based on the data of a single detector at 150 GHz, while a more detailed analysis covering four 150 GHz detectors and a larger data set was later presented [163]. Maxima, conceived as a follow-up of MAX, was a bolometric receiver, cooled at 100 mK by an adiabatic demagnetisation refrigerator, sensitive to multipoles  $80 < \ell < 800$  with frequency bands centred at 150, 240, and 410 GHz. The first flight in its full configuration [164] was launched in August 1998, and covered 0.3% of the sky (3200 independent pixels) during a 7-hour conventional flight. The Boomerang and Maxima power spectrum measurements were in agreement for what concerns the first-order key features: both showed clear evidence of a peak  $\ell \sim 200$  (corresponding to a density parameter  $\Omega_0 \sim 1$ ), and indications of further acoustic features at higher multipoles [165]. More recently, the Archeops experiment [166] obtained accurate measurements over the multipole range 15–350 with an array of 21 bolometers in the

140–550 GHz range cooled at 100 mK with an arctic balloon flight covering 30% of the sky, and yielded accurate power spectrum data bridging between COBE and the first acoustic peak.

## 5.3 WMAP

### 5.3.1 Mission summary

The original idea of the Microwave Anisotropy Probe was conceived in the early 90’s. After the loss of Dr. David Wilkinson, a member of the science team and pioneer in the study of the CMB occurred during the first year data acquisition, the satellite was renamed Wilkinson Microwave Anisotropy Probe (WMAP).

The primary science goal of WMAP is to map the relative CMB temperature over the full sky with an angular resolution corresponding to a pixel side of about 0.3 degrees, a sensitivity of 30  $\mu$ K per square pixel, with a contribution from systematics limited to 5  $\mu$ K per pixel. As we discuss below, the entire design of the instrument was conceived in order to achieve control of foreground emission and systematics.

WMAP (see Fig. 9) consists of two back-to-back Gregorian telescopes (1.4 m  $\times$  1.6 m primary and 0.9 m  $\times$  1.0 m sub-reflector) coupled to two symmetric focal planes with 10 radiometers each. Two sky signals coming from directions separated by a total angle of  $141^\circ$  are compared by pseudo-correlation receivers at five different frequency bands centred at 22.8, 33.0, 40.7, 60.8, 93.5 GHz with FWHM beamwidths respectively of 0.82, 0.62, 0.49, 0.33, 0.21 degrees [120].

The signal collected by a corrugated feed horn is split into two orthogonal polarisation modes by an Ortho-Mode Transducer (OMT). Each polarised component is combined with the orthogonal component coming from the symmetric channel in the opposite focal unit and then amplified by passively cooled (at  $\sim 100$  K) High Mobility Electrons Transistor (HEMT) amplifiers. After a second warm amplification, signals are phase-shifted and then split back into the two original input signals, detected and then differenced. This differential setup is common to many high sensitivity CMB microwave detectors and provides reduced  $1/f$  noise and contamination by amplifiers instabilities with respect to other radiometer chain configurations. For example the  $1/f$  knee frequency,  $f_k$ , of WMAP radiometers is typically  $< 50$  mHz and for half of them it is below 1 mHz. WMAP main instrumental performances are summarised in Tab. 1; for more details, see [167] and visit <http://map.gsfc.nasa.gov>.

Table 1: A summary of the WMAP nominal features.

Band	K	Ka	Q	V	W
Centre frequency (GHz)	23	33	41	61	94
Bandwidth (GHz)	5.5	7	8.3	14	20.5
Equivalent FWHM (deg.)	0.93	0.68	0.53	0.35	0.30
Sensitivity ( $\mu$ K 0.3 deg. $\times$ 0.3 deg. pixel)	35	35	35	35	35
Number of detectors	4	4	8	8	16

The observation orbit is located at the L2 Sun-Earth Lagrange point, 1.5 million km from

## Asked permission for publication

Figure 9: An overview of the WMAP satellite, showing the double-telescope system, the large radiators, and the satellite service module with deployable solar panels on the bottom. One of the two focal arrays of feed horns is also partially visible on the right. The overall height is 3.6 m, the mass is 830 Kg and the diameter of the deployed solar panels reaches 5.1 m. The solar arrays supply a 400 Watts power to the spacecraft and instruments (with permission, courtesy of the NASA/WMAP Science Team).

Earth. The WMAP observation direction is constantly away from the Sun, Earth and Moon, with a scanning strategy that allows to observe the full sky every six months. This ensures a high thermal stability with no active cooling stages and negligible radio frequency interference from the Sun, Earth and Moon. The observational strategy (see Fig. 10) is based on fast precessions ( $\sim 0.34$  mHz) of the spacecraft, spinning at 0.464 rpm (7.57 mHz); as a consequence approximately 30 % of the sky is observed each hour and the sensitivity pattern is effectively smoothed.

The data were calibrated by comparing the raw voltage output from the differential radiometer with the known cosmic dipole signal; the WMAP map making procedure is based on a technique already used for COBE [126]. The final map,  $X$ , is obtained iteratively:

$$X^{n+1} = X^n + D^{-1}[B - AX], \quad (17)$$

where  $A = \sum_t P^T(t)P(t)$  is sum over all the observation times of the time dependent pointing vector  $P(t)$  times its transposal,  $B = \sum_t V(t)P(t)^T$  with  $V(t)$  representing the time ordered data and  $D$  a diagonal matrix with the number of observations at each sky pixel in the diagonal

elements. WMAP adopted the HEALPix sky pixelisation scheme [168].

## Asked permission for publication

Figure 10: The WMAP scan strategy (with permission, courtesy of the NASA/WMAP science team).

### 5.3.2 Discussion of first-year results

The recent data release of the first year of WMAP observation is, no doubt, the most important event in CMB anisotropy study since COBE, a few months after the first evidence of a polarised signal by DASI [155].

The WMAP frequency coverage allows a quite good removal of the astrophysical foregrounds, in particular of the Galactic components that are more crucial at the multipoles ( $\ell \lesssim 800$ ) where the WMAP sensitivity is high enough to accurately measure the CMB power spectrum and main beam distortion effects are not crucial.

The first step [169] in this subtraction has been the construction of several masks, based on asymmetric tail at positive signals of the histogram of the pixel values at 22.8 GHz, to be applied to the full sky maps according to the desired maximum level of signal to be excluded from the analysis. This step is then complemented by excluding sky regions selected for high contamination by bright discrete sources, identified by exploiting several source catalogues.

Then, three different and complementary approaches were pursued to separate CMB anisotropy from Galactic foregrounds, providing quite consistent results. The first one, which has the advantage to be based only on WMAP data themselves, searches a linear combination of the frequency maps using weights aimed at reproducing the planckian shape of the CMB spectrum. The second one, recognised by the WMAP team as the best to reconstruct the CMB anisotropies, is based on fitting the WMAP frequency maps with the templates of Galactic emission obtained at radio (for the synchrotron emission) or at Far-IR (for the thermal dust emission) bands and on the  $H\alpha$  emission (for the free-free emission). Finally, these templates can be used as inputs for a MEM component separation of WMAP frequency maps, a third method claimed by the authors as the best to derive Galactic diffuse emission maps.

A good correlation has been found between the free-free WMAP template and the map of  $H\alpha$  emission. The relatively flat spectral index of the synchrotron emission ( $\sim -2.5$ ) close to the Galactic plane supports the idea of a significant diffusion and convection of cosmic rays associated to recent star formation, while the steeper spectral index ( $\sim -3$ ) at high Galactic latitudes suggests the relevance of diffusion and that cosmic-ray electrons are trapped in the halo for a timescale long enough to lose a relevant fraction of their energy. The steep thermal dust spectral index ( $\sim -2.2$ ) found at WMAP frequencies possibly implies a significant contribution from silicate grains. The overall level of the Galactic emission at WMAP scales has been confirmed to be minimum at frequencies about 70–80 GHz while upper limits of about 5 % (at 22.8 GHz) have been estimated for the contribution of spinning and magnetic dust emission. Finally, the angular power spectrum of Galactic emission at all WMAP frequencies is approximately  $\propto \ell^{-2}$  and the same holds for each of the three most relevant components, indicating a strong correlation among them. This slope, in agreement with that derived from Far-IR maps, is flatter than that derived from the Haslam map (about  $\propto \ell^{-3}$ ).

In spite of its quite poor sensitivity at small angular scales ( $\ell \gtrsim 700$ ), WMAP provided also interesting results on discrete extragalactic sources and on their confusion noise. By cross-checking on several radio catalogues or directly by identifying sources in the WMAP maps by dedicated filters, density fluxes of about two hundreds radio sources (the large majority of them showing a quite flat spectrum) have been measured. The corresponding level of confusion noise derived by the authors is in good agreement with the  $C_\ell$  value at  $\sim 40$  GHz of the model by Toffolatti et al. [93], as well as the number counts at fluxes above 1–2 Jy that seems to favour the lowest predictions of this model, while smaller scale experiments (CBI, VSA), sensitive to fainter sources, are in a more strict agreement with its mean predictions. Finally, although some thermal SZ effect toward some bright cluster has been clearly detected by WMAP, the global SZ contamination is found to be negligible in the WMAP first-year maps.

The main scientific product of the WMAP data consists in the angular power spectrum of CMB temperature anisotropies and of the cross correlation between temperature and  $E$  polarisation modes (see Fig. 11 [25]). The sky maps used for the computation of the power spectra have been obtained by cross correlating the 60 GHz and the 90 GHz channels, in order to reduce systematics effects, and excluding the galactic plane from the analysis to minimise the foreground signal contamination.

The basic approach of the WMAP team in getting the best cosmological model fit is a Bayesian analysis assuming flat priors, obtaining the parameters characteristic of the best fit model from the maximum of the likelihood surface [25]. For each parameter, the one dimensional likelihood is also constructed, by marginalising over all the other parameters. A first parameter estimation is done with respect to a basic cosmological model ( $\Lambda$ CDM), with zero spatial curvature, radiation, baryonic matter, cold dark matter and a cosmological constant.

It turns out that the temperature-temperature (TT) and temperature-polarisation (TE) cross correlations, as measured from WMAP only, are well fitted by a set of values for the basic cosmological parameters which is summarised in Tab. 2 (each value is given at  $2\sigma$  confidence level). It is important to note that the combination of polarisation and temperature data has a fundamental role in reducing the uncertainty in the parameter estimation. One of the most

relevant results is that the TE cross correlation appears to favour high optical depth values, indicating an early reionisation process; however, if the spectral index  $n_s$  is assumed to be scale-independent, the likelihood is quite flat with respect to variations of these two parameters, because the observed low amplitude of fluctuations at low multipoles disfavors the additional large scale anisotropies which would be produced by reionisation. The degeneracy is alleviated by assuming a running spectral index.

Table 2: Main cosmological parameters estimated from WMAP first year data

Parameter		Mean ( 68% confidence range)	Maximum Likelihood
Baryon Density	$\Omega_b h^2$	$0.024 \pm 0.001$	0.023
Matter Density	$\Omega_m h^2$	$0.14 \pm 0.02$	0.13
Hubble Constant	$h$	$0.72 \pm 0.05$	0.68
Amplitude	$A$	$0.9 \pm 0.1$	0.78
Optical Depth	$\tau$	$0.166^{+0.076}_{-0.071}$	0.10
Spectral Index	$n_s$	$0.99 \pm 0.04$	0.97
	$\chi^2_{eff}/\nu$		1431/1342

The WMAP temperature and polarisation data have been combined with recent CMB data on smaller angular scales, and with complementary and independent data from large scale structure (weak lensing, velocity fields and clusters abundance, Lyman- $\alpha$  forest) and Type Ia Supernovae, as well with measurements of the Hubble constant (see [25] and references therein). In addition to the simpler  $\Lambda$ CDM, more complex cosmological models (non-flat universes, Dark Energy models, models with tensor perturbations, and models with massive neutrinos) have also been considered; each of them required Monte Carlo simulations to explore the likelihood surface. Obviously, increasing the complexity of the cosmological model introduces additional parameters, and possibly new degeneracies in the parameter space at the WMAP resolution.

When WMAP data are combined with independent datasets, it is possible to constrain significantly the additional parameters in the model under investigation, as in the case of a Dark Energy model with constant equation of state  $w$ : in this case, the combination of CMB data and Supernovae or large scale structures, place a  $2\sigma$  limit on  $w < -0.78$ . In general, it has been found a noticeable agreement between WMAP data and most of the independent astrophysical datasets.

The remarkable observational convergence made possible to build a “concordance model” of the Universe, i.e. the currently accepted cosmological scenario: incontrovertible evidence has accumulated in favor of an almost flat Universe, with 70% of its energy density made by the Dark Energy, a cosmological component responsible for the acceleration in cosmic expansion, opening a new era for theoretical and fundamental physics; the quite high value of the Hubble constant, as determined by independent observations, forces the present Dark Energy equation of state to be close to  $-1$  (the value typical of the cosmological constant); the standard Big Bang scenario received further powerful confirmation by the remarkable agreement between the

baryon density inferred from the Deuterium/Hydrogen abundances ratio and the relative height of the CMB temperature anisotropy.

Despite the agreement between WMAP data and the predictions of the “concordance” model, a note of caution should be done about the “anomalies” found in the power spectrum: in particular, WMAP confirmed the COBE evidence for a lower-than-expected amplitude for the temperature quadrupole and octupole anisotropies. It is still a controversial question whether this apparent discrepancy between data and predictions requires a new physics, or it can be simply interpreted as a systematics artifact or just a low-probability realisation of the Universe. A detailed investigation of the statistical significance of the low-multipole values of the temperature anisotropies can be found in [170].

A CMB “imager” like Planck, i.e. an instrument capable to image the primordial CMB anisotropies being signal dominated even at its highest resolution of a few arcmin, will allow a deep investigation of the physical nature of the concordance model assessed by WMAP and other astrophysical observations. In particular, the detail in the CMB anisotropy pattern will spread light on the possible primordial non-Gaussianity, allowing to discriminate between inflationary models, as well as on the nature of the 96% dark component in the Universe, through the shear induced by forming structures at the onset of the dark energy dominated era.

## Asked permission for publication

Figure 11: TT and TE cross power spectra for WMAP, COBE, CBI and ACBAR data; the solid line corresponds to the WMAP best fit model [25] (with permission, courtesy of the NASA/WMAP science team).

### 5.4 Planck

#### 5.4.1 Objectives, and expected performances

The Planck mission of the European Space Agency is the third generation space mission dedicated to the measurement of CMB anisotropies. Planck is designed to *fully* extract the cosmological information contained in CMB anisotropy by setting angular resolution, spectral coverage and sensitivity such that the power spectrum reconstruction will be limited by unavoidable cos-

mic variance and astrophysical foregrounds. Planck will also provide a precise measurement of the TE correlation and of the E-mode polarisation power spectrum and possibly offer a first B-mode detection.

In order to achieve these ambitious goals, several, highly stringent performance requirements need to be satisfied by the instruments and the satellite (see Tab. 3): full sky coverage (to minimise sample variance at low multipole values), angular resolution  $\lesssim 10'$  (to measure the power spectrum up to the “Silk damping” region), noise per pixel  $\lesssim 10 \mu\text{K}$  (to minimise the statistical uncertainties in the whole multipole range), wide frequency coverage (to ensure accurate foreground separation), control of systematic effects at the  $\mu\text{K}$  level.

Table 3: Main instrumental performances of Planck mission.

		<i>LFI</i>	<i>HFI</i>
Angular resolution		33'–13'	9.2'–5'
Avg. $\Delta T/T$ per pixel <sup>a</sup> (1 year mission) <sup>b</sup>	Intensity	$6.5 \times 10^{-6}$	$2.0 \times 10^{-6}$
	Polaris. <sup>c</sup>	$9.2 \times 10^{-6}$	$4.2 \times 10^{-6}$
Baseline mission lifetime		14 months	14 months
Spectral coverage		30–70 GHz	100–857 GHz
Detector technology		HEMT	Bolometers
Detector temperature		20 K	0.1 K
Cooling		Active	Active

<sup>a</sup> The sensitivity in thermodynamic temperature and refers to the 70 GHz LFI and to the 100 GHz HFI for on a 10' pixel. A pixel is a square whose side is the FWHM extent of the beam.

<sup>b</sup> These figures are calculated for the average integration time per pixel. In general the integration time will be inhomogeneously distributed on the sky and will be much higher in certain regions.

<sup>c</sup> Refers to E-mode polarisation (Stokes parameters U and Q).

The angular resolution is obtained with a 1.5 m aperture primary mirror, while the optimal optical response is offered by a combination of an off-axis dual reflector aplanatic telescope and dual-profiled corrugated feed horns in the focal plane to maximise beam symmetry and minimise sidelobe pick-up (see Sect. 4.2).

The most effective removal of astrophysical foregrounds will be guaranteed by a wide frequency range, spanning from 30 GHz to  $\sim 900$  GHz. Such a wide frequency range calls for the implementation of different detector technologies, i.e. HEMT radiometric receivers for the frequency range 30–70 GHz (the LFI instrument) and bolometric detectors for the frequency range 100–900 GHz (the HFI instrument).

The required sensitivity will be reached by a combination of wide-band components (20% of the centre frequency for Planck-LFI, 30–40% for HFI), long integration times (14 months of nominal mission time) and multiple cryogenically-cooled detectors. In particular the front-end amplifiers of the LFI instrument will be actively cooled at  $\sim 20$  K, while the HFI bolometers will operate at  $\sim 0.1$  K.

The presence of a complex cryogenic chain and the need of a tight control of systematic effects has imposed the development of a satellite and instrument thermal design with high stability performances. The thermal design and orbit selection will guarantee the necessary stability to maintain the residual systematic effects at levels well below the instrument sensitivity.

#### 5.4.2 Mission concept

**Satellite and scanning strategy design.** A schematic picture of the Planck satellite is shown in the left panel of Fig. 12. The satellite is composed by two main modules: the payload module (PLM) with the telescope and the instruments in the focal plane and a Service Module (SVM) that houses the compressor systems of the on-board coolers and all the instrument and satellite warm electronics and subsystems. Three thermal shields of conical shape (called V-Grooves) at  $\sim 150$  K,  $\sim 100$  K and  $\sim 50$  K thermally decouple the passively cooled payload (at  $\lesssim 60$  K) from the warm SVM (at  $\sim 300$  K). The necessary power is provided by the solar panels located on the back of the SVM which are always oriented toward the Sun during the survey.

After launch Planck will reach a nearly circular orbit ( $\sim 200.000$  Km diameter) around the L2 Lagrangian point of the Sun-Earth system, at about 1.5 MKm from Earth, to maintain the focal plane instruments constantly in shadow with the sky in full view and the satellite with a very high degree of thermal stability.

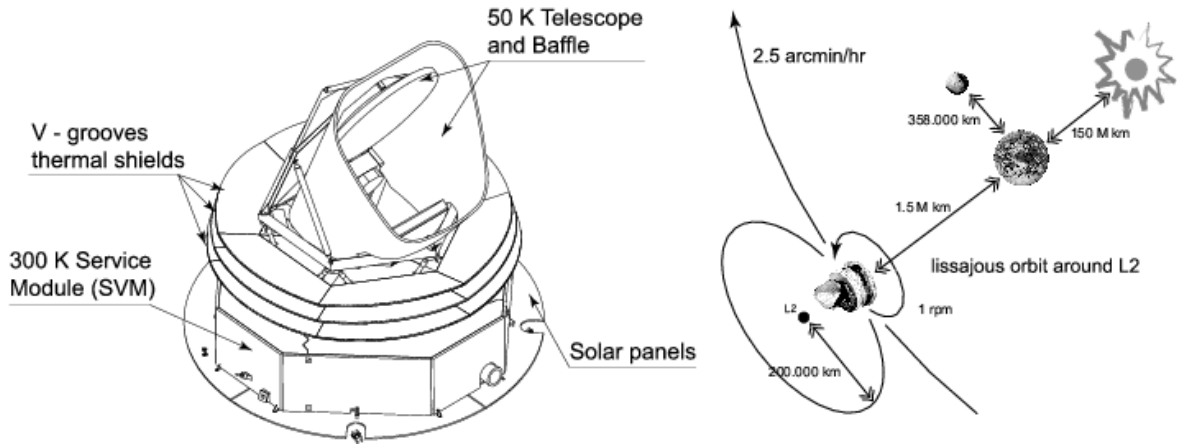


Figure 12: Left panel: a schematic of the Planck satellite showing the payload (with telescope and focal plane instruments), the warm service module and the three V-grooves that thermally decouple the cold from the warm satellite stages. The telescope includes the primary reflector with its supporting structure, the secondary reflector with its fixation struts, the telescope frame (holding the two mirror support structures, the focal plane unit and the interfaces with the payload module struts), the payload module straylight baffle (interfaced with the coldest V-groove shield at 50 K), the telescope inner baffle between the focal plane array and the secondary mirror, the primary reflector extension baffle, the instrumentation for the telescope hardware, and the hardware interfaces with the instruments. Right panel: sketch of the nominal Planck scanning strategy.

In the right panel of Fig. 12 we show a sketch of the nominal Planck scanning strategy. Planck will spin at  $\sim 1$  r.p.m., scanning the sky in nearly great circles with the telescope line-of-sight pointing at  $85^\circ$  with respect to the spin axis. Hourly maneuvers will re-point the telescope by about  $\sim 2.5$  arcmin to maintain the spin axis constantly aligned with the Sun and the Earth. With this strategy each sky circle is scanned approximately sixty times before repointing (thus providing large redundancy over each scanned circle) and the whole sky is covered in about six months of continuous observations. The satellite also offers the possibility to oscillate or precess the spin axis in order to increase the number of “crossings”<sup>5</sup> and facilitate the removal of residual systematic effects from the data stream during data processing. The definitive details of the scanning strategy are not frozen yet. Because Planck will cover the sky twice, it is possible that the scanning laws of the two surveys will be different in order to optimise coverage and systematics rejection.

**Telescope optical design.** The Planck telescope represents a challenge for telescope technology and optical design, because of the wide frequency coverage, the high performances required by both HFI and LFI instruments sharing a very large  $400 \times 400$  mm focal region, and the cryogenic environment (40–65 K) in which the telescope will operate. Its optical design is based on a two-mirror off-axis scheme (see Fig. 13) which offers the advantage to accommodate large focal plane instruments with an unblocked aperture, maintaining the diffraction by the secondary mirror and struts at very low levels.

Both the primary and the secondary mirrors have an ellipsoidal shape as in the case of the Gregorian aplanatic design [107, 108]. The primary mirror physical dimensions are  $\sim 1.9 \times 1.5$  m, allowing a projected circular aperture of 1.5 m diameter. The secondary reflector has been oversized up to approximately 1 m diameter to avoid any additional under illumination of the primary.

The mirrors will be fabricated using Carbon Fiber (CFRP) technology. The baseline consists of an all-CFRP rounded triangular tubes sandwich array arranged in a honeycomb-like structure. This kind of structure has been chosen to satisfy the requirements of low mass ( $< 120$  Kg including struts and supports), high stiffness, high mechanical accuracy, and low thermal expansion coefficient. The sandwich concept consists of a thick (4–10 cm) honeycomb-like core with the desired shape, and to which two thin ( $1 - 1.5 \mu\text{m}$ ) reflecting skins are bonded.

**Focal plane instruments.** Two complementary instruments are housed in the Planck focal plane (see Fig. 14): the Low Frequency Instrument (LFI) covering the 30–70 GHz range and the High Frequency Instrument (HFI) covering the 100–857 GHz range. LFI is an array of coherent, differential radiometers based on cryogenic InP HEMT amplifiers operated at  $\sim 20$  K. To minimise power dissipation in the focal plane the radiometers are split into two sub-assemblies connected by a set of custom designed waveguides.

---

<sup>5</sup>With the term “crossings” we denote the pixels in the sky that are measured by a single detector during two different scan circles. These crossings are useful during data reduction to recognise and possibly remove instrumental systematic effects that may be present in the measured data stream.

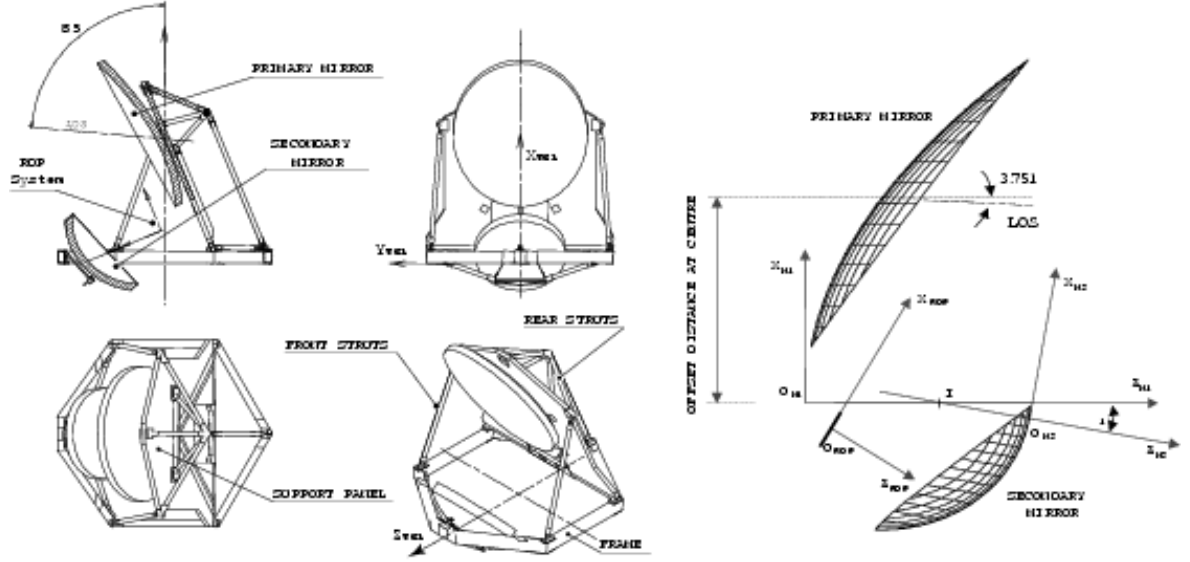


Figure 13: Telescope Design. Left: different views of the telescope mechanical layout. Right: telescope coordinate systems.

The radiometers use a pseudo-correlation scheme to suppress  $1/f$  noise induced by amplifier gain and noise temperature fluctuations [121]. The differential measurement is taken comparing the sky signal against a stable internal cryogenic reference load cooled at  $\sim 4$  K, taking advantage of the pre-cooling stage of the bolometric instrument. In addition, in LFI the effects of the residual input offset ( $\lesssim 2$  K in nominal conditions) is compensated by introducing a *gain modulation factor* [95] which balances the output in the on-board signal processing and greatly improves the stability of the measured signal.

Current LFI prototypes establish world-record performances in the 30–100 GHz range for noise, bandwidth and low power consumption. The amplifiers at 30 and 44 GHz are incorporated into a microwave integrated circuit (MIC) [171]. At these frequencies the parasitics and uncertainties introduced by the bond wires in a MIC amplifier are controllable, particularly given the relatively low number of channels (total of 10), and the additional tuning flexibility facilitates optimisation for low noise. The LFI amplifiers have demonstrated noise temperatures  $\sim 7.5$  K at 30 GHz with 20% bandwidth. At 70 GHz there will be 12 channels [172]; amplifiers at these frequencies will use MMICs (monolithic microwave integrated circuits), which incorporate all circuit elements and the HEMT transistors on a single InP chip, so that the amplifiers can be mass-produced in a controlled process. Cryogenic MMIC amplifiers have been demonstrated at 75–115 GHz which exhibit  $< 35$  K over the required bandwidth. The LFI will thus fully exploit both MIC and MMIC technologies at their best. The LFI is “naturally” polarisation-sensitive in all of its channels, with a sensitivity to the Q and U Stokes parameters  $\sim \sqrt{2}$  lower compared to temperature anisotropy.

The spectral region above 100 GHz is covered by the High Frequency Instrument (HFI),

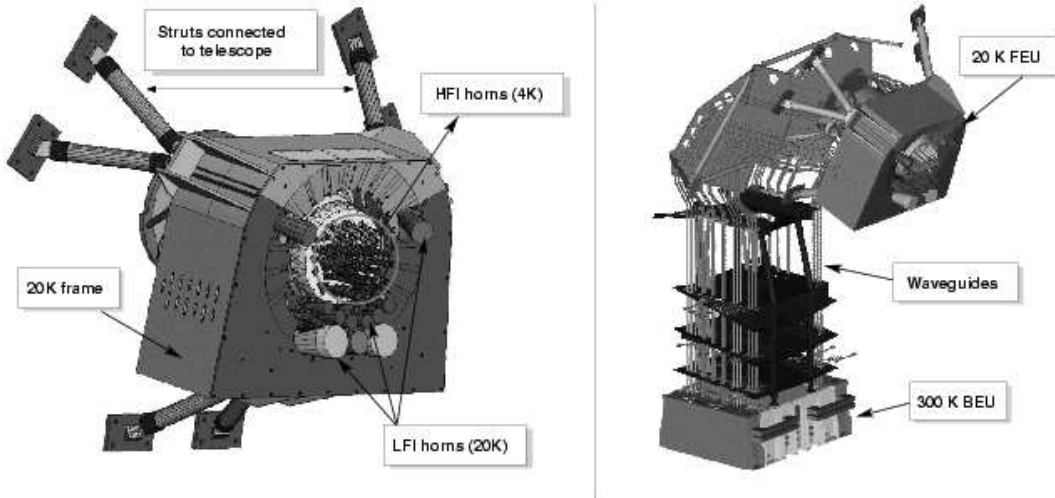


Figure 14: Left: view of the instruments in the Planck focal plane. The LFI horns surround the HFI instrument located in the centre of the focal surface. Right: view of the integrated LFI-HFI assembly. A set of 48 waveguides connect the front-end part of the LFI radiometers (FEU) to the warm back-end unit (BEU).

consisting of an array of 48 spider-web bolometers operated at 0.1 K, and distributed in 6 frequency bands from 100 to 850 GHz [173]. Cooling the bolometers down to 0.1 K in space is a key driver in the design of the instrument and spacecraft. After the 50–60 K passive cooling and the 18–20 K stage (shared with LFI), the HFI cryo-chain uses a mechanical cooler to provide a 4 K stage (also used by LFI to cool the reference loads). The 4 K cooler is designed to minimise microphonic effects, and it operates at a frequency near 40 Hz adjustable in-flight to minimise resonances. Finally, a  $^3\text{He}$  -  $^4\text{He}$  closed-cycle dilution cooler provides 0.1 K temperature to the bolometers.

The focal plane is constituted by an array of back-to-back horns at 4 K with spectral filters placed at  $\sim 1.6$  K, and a third horn re-images radiation onto the bolometric detector [174]. For the HFI 100, 143 and 217 GHz channels, single-mode propagation is used. For these channels, as well as for LFI, the feed horns use double-profiled corrugated design to optimise telescope illumination and edge taper. At higher frequencies the angular resolution is achieved without diffraction-limited conditions, and multi-moded horns are being employed.

Extraordinary sensitivities ( $NEP \sim 1 \times 10^{-17} \text{ W} \times \text{Hz}^{-1/2}$ ) are achievable with HFI, and have been demonstrated by prototype measurements. Thermal stability requirements are proportionally stringent, at sub- $\mu\text{K}$  in the 0.1 K stage environment. The use of “spider-web” bolometer technology [175, 176], with silicon nitride micro-mesh, can provide nearly background-limited performance. Originally designed as a temperature sensitive instrument only, HFI has been modified to include polarisation sensitive bolometers (PSBs) [177] in a subset of the channels (100–350 GHz), allowing sensitive polarisation measurements at these frequencies. The HFI PSBs are built so that two absorbers made with parallel wires coupled to orthogonal polari-

sation modes are located in the same cavity and share the same feed horn, filter and optical path.

**Cryo-chain.** The performance of the ultra-high sensitivity detectors required for the Planck mission is strongly coupled to their temperature. This implies that operating temperatures need to be reached and maintained for the whole mission duration while temperature stability and possible thermal noise due to the cryogenic systems must be controlled to the most accurate level.

The Planck thermal and cryogenic design is one of the most complex ever conceived. The global architecture of the Planck cooling system (shown in right panel of Fig. 15) can be summarised as follows:

- Solar Array and SVM shield at 300 K to shield the payload from the sun.
- Pre-cooling for all active coolers from 300 K to  $\sim 60$  K by means of passive radiators in three stages ( $\sim 150$  K,  $\sim 100$  K,  $\sim 60$  K) [178].
- Cooling to 18–20 K for LFI and pre-cooling for the HFI 4 K cooler with a  $\text{H}_2$  Sorption Cooler [179, 180, 181, 182].
- Cooling to 4 K with a Helium Joule-Thomson cooler with mechanical compressors, as pre-cooling stage for the dilution refrigerator [183].
- Cooling down to 1.6 and 0.1 K with an open loop  $^4\text{He}$ - $^3\text{He}$  dilution refrigerator [184, 185].

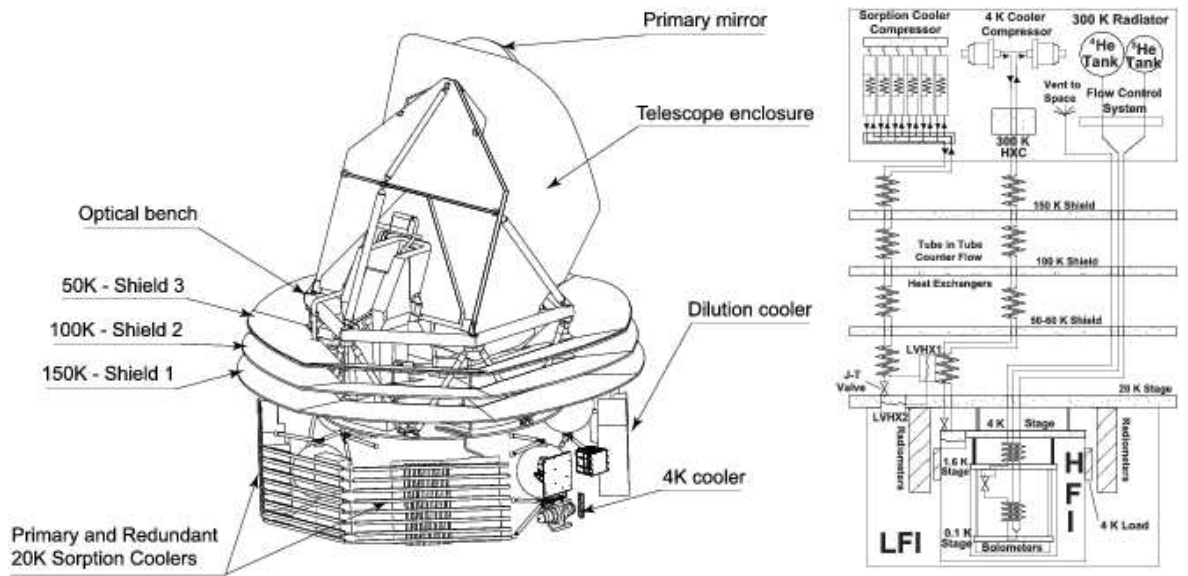


Figure 15: Left: The Planck spacecraft passive radiators scheme and the location on the spacecraft of the three active coolers. Right: schematic of the Planck Cryogenic Chain.

In the thermal environment of the Earth-Sun Lagrangian L2 orbit, the Sun is the major source of radiation: the combined action of the sun-shield/solar array and the SVM shield allows to keep the spacecraft in constant shadow. The cold payload is thermally decoupled from the warm SVM by low conductance struts and thermal radiators (the so-called V-Grooves, see left panel in Fig. 15).

The three V-Grooves are characterised by low-emissivity specular surfaces with an open angle of a few degrees between each shield, allowing an extremely efficient heat rejection to space [178]. The coldest radiator, with a surface of only 3-4 m<sup>2</sup>, is capable of rejecting up to 2 W at 60 K. On the other side, V-Groove shields impose geometrical constraints and increase integration complexity.

Below 60 K a dedicated active refrigeration system allows to reach and maintain the operating temperatures for the two instruments, while minimising oscillations and thermal effects. The Planck cryogenic chain is driven by the H<sub>2</sub> Sorption Cooler [179], a closed-cycle cryo-cooler designed to provide 1.2 Watt of heat lift at a temperature of  $\sim 18$  K using isenthalpic expansion of hydrogen through a Joule-Thompson (JT) valve. The Sorption Cooler performs a simple thermodynamic cycle based on hydrogen compression [180], gas pre-cooling by three passive radiators, further cooling due to the heat recovery by the cold low pressure gas stream, expansion through a J-T expansion valve and evaporation at the cold stage. The engine of the Planck Sorption Cooler is the compressor system, based on the intrinsic property of a metal hydride alloy (namely La<sub>1.0</sub>Ni<sub>4.78</sub>Sn<sub>0.22</sub>) to absorb large quantities of low-pressure hydrogen and to desorb it at high pressure when heated in a limited volume [181]. The compressor system, with no moving parts, is made of six elements, each containing the sorbent material which is periodically cycled between heating and cooling phases: their cycle phases are staggered in order to produce a continuous stream of liquid refrigerant [182]. In such a system, there is a basic clock time period over which each step of the process is conducted: since each phase lasts 667 seconds, the cooler total cycle time is  $\sim 4000$  s.

The gas leaves the compressor with a flow of 6.5 mg/sec, pressurised at 4.8 MPa: this high-pressure hydrogen at  $\sim 300$  K is then pre-cooled below the inversion temperature by the combination of cold low-pressure return flow and the three V-Grooves. The temperature of the coldest V-Groove determines the available heat lift of the cooler. After Joule-Thompson expansion, the gas will partially liquefy, producing low pressure liquid refrigerant. The saturated liquid-vapour hydrogen mixture is collected into two Liquid-Vapour Heat Exchangers, LVHX-1 and LVHX-2, which interface to HFI and LFI, respectively. Heat evaporates liquid hydrogen and the low-pressure gaseous hydrogen is re-circulated back to the sorbent for compression. In order to minimise the temperature oscillations at the interface plate with the LFI, a Temperature Stabilisation Assembly (TSA), based on an active PID control loop, is implemented on the LVHX2.

The Planck lowest temperature stages (1.6 K and 0.1 K) are reached by the 0.1 K Open Cycle Dilution/Joule-Thomson Refrigerator, which requires the gas to be pre-cooled at a temperature lower than 10 K. This task is performed by a closed cycle 4 K Joule Thomson (JT) Cooler [183]. This refrigerator uses <sup>4</sup>He as a fluid, pressurised by a pair of mechanical compressors mounted back-to-back and controlled by low vibration drive electronics with force transducers

and a servo feedback loop to minimise the transmitted vibrations. Part of the heat lift produced by the Sorption Cooler is used to cool helium down to 18 K by high-efficiency heat exchangers.

The dilution refrigerator exploits a new dilution principle based on friction that does not need gravity to operate [184]. Its cooling power depends on the low gas flow, which allows enough gas storage to achieve long mission life [185]. For a total ( $^3\text{He}$  and  $^4\text{He}$ ) flow rate of  $12\ \mu\text{mole/s}$ , a cooling power of 100 nW at 0.1 K has been demonstrated. In the same process, the mixture is expanded in a Joule-Thomson valve, producing a cooling power of several hundreds of mW at 1.6 K. This is enough to ensure a proper insulation of the 0.1 K stage from the radiative and conductive thermal loads coming from the 4 K stage. The 1.6 K stage supports filters and intercepts heat from the 4 K stage. The 0.1 K stage refrigerates the bolometers, thermometers, heaters, and filters. Its temperature is controlled by a closed loop active system. The tubes from and to each stage are attached to form heat exchangers for all circulating fluids in order to minimise thermal losses.

**Calibration.** Photometric calibration is necessary to convert the receiver output (arbitrary digitised telemetry units) to the corresponding observed temperature of the sky (“absolute calibration”) and to monitor variations of such conversion with time (“relative calibration”) to compensate for instrumental drifts.

Calibration needs to be performed accurately and frequently, to control the instruments behaviour. It is a crucial operation since errors in this procedure may create artifacts and errors in the amplitude of detected structures in the final maps. Calibration uncertainty is one of the most significant systematic errors affecting current CMB anisotropy experiments. The measurement accuracy sought by precision space experiments requires a calibration accuracy at the level of  $\sim 1\%$  in order to derive the CMB power spectrum with comparable accuracy [134].

Calibration is typically performed by observing celestial sources with known intensity, such as planets, strong radio sources or the CMB dipole.

For the Planck instrument, relative calibration is performed every hour, thanks to the adopted scanning strategy. Bright sources (e.g. HII regions at lower frequencies, or planets) are very useful in this respect, when available. This allows to establish calibration between individual scans, before and independently of establishing an absolute calibration for all data. Absolute calibration is performed on different time scales. On short time scales, it mainly relies on the CMB dipole induced by the motion of the solar system, which is known at 0.4% level thanks to the COBE-FIRAS measurement [6] and on the strong signal from the galactic plane [134]. On long time scales ( $\sim 3$  months), it relies on the dipole modulation of the signal induced by the motion of the Earth (and consequently of the satellite) around the Sun.

**Foregrounds removal.** As already mentioned in Sect. 3, any CMB experiment observes together with the CMB other foreground sources of astrophysical origin. These sources have in general a different spectral and spatial behaviour than the CMB and this fact will, in principle, allow proper separation of the various contributions. However the strong accuracy requirements of present and future CMB missions makes this a non trivial issue. In this respect a multi-frequency experiment with optimal spacing between frequencies is the first step for a proper

separation of the sky components. Furthermore algorithms that allow effective foreground separation from measured maps are needed.

These algorithms can be divided into two main categories: the so-called “blind” algorithms and those that require some a-priori knowledge on the components to be separated. The Maximum Entropy Method (MEM) [186, 187] is an example of the latter category that has been developed and already applied, both in real and in harmonic space, to Planck-like data-sets. The priors can be in the form of spectral indexes of the components or their spatial behaviour. The Expectation Maximisation (EM) [188] and the Fast Independent Component Analysis (FASTICA) [189], instead, are blind schemes that have also been applied to astrophysical data-sets. FASTICA, in particular, needs no assumptions either on the spectral or on the spatial dependences of the components but it requires only their statistical independence and the non Gaussianity of all (but one) components. This condition is easily fulfilled in CMB foreground separation where all the components are independent and CMB is expected to be Gaussian while foregrounds are not. FASTICA has been applied to both simulated Planck-like data [189] as well as to real data (e.g. on COBE-DMR [88]). An implementation in harmonic space is under way with the possibility of a further improvement in the separation.

**Data Processing Centres.** To correctly perform the calibration and foreground removal phases, fundamental for the proper scientific exploitation of the mission, a whole set of preparatory and merging work on the Planck data needs to be accomplished. These activities range from the receipt of the telemetry sent by the satellite to the actual delivery of the final scientific results of the mission to the European Space Agency, through a number of processing steps defining a “pipeline”. Such activities are carried out by two separate but coordinated Data Processing Centres (DPCs), one for each of the Planck instruments.

The DPCs are responsible for the operations of their own instrument, and for the production, delivery and archiving of the scientific data products, which can be considered as the deliverables of the mission. Such products include calibrated time series data for each receiver after removal of systematic features and attitude reconstruction; photometrically and astrometrically calibrated maps of the sky in the observed bands; sky maps of the main astrophysical components; catalogues of sources detected in the sky maps of the main astrophysical components. The DPCs are furthermore responsible for the production of realistic data simulating the behaviour of the instrument in flight, and for the support to instrument testing on the ground.

During the pre-launch era, the DPC is built by integrating and making operational at a single site, within a data processing pipeline, a set of input algorithms implemented by scientists distributed throughout a dozen different countries. During flight, the DPC main efforts will be concentrated on controlling their instruments and achieving the best possible performances, through a detailed analysis of their behaviour and preliminary processing of scientific data. In the post-operations phase, the processing procedures will be finalised, and the whole pipeline will be run on all of the data, from telemetry handling down to the scientific analysis of the mission results, and delivery to the scientific community.

## 5.5 Current status

With the release of the 1 year results from WMAP we enter the era of precision cosmology. WMAP clearly detected acoustic oscillations in the CMB temperature power spectrum with cosmic-variance accuracy up to  $\ell \simeq 350$ . Correlation between temperature and polarisation  $E$ -modes have been also reported which is able to better constraint the re-ionisation epoch of the Universe. The main result is that a flat  $\Lambda$ -dominated Universe seeded by a nearly scale-invariant adiabatic Gaussian fluctuations is a very good fit to the WMAP data and a series of other astronomical observations. When combining WMAP data with those from smaller scales CMB experiments (CBI [190] and ACBAR [157]) with large scale structure measurements from 2dFGRS [191] and  $\text{Ly}\alpha$  power spectrum [192, 193], the data yield the values for the basic cosmological parameters reported in Tab. 4.

Table 4: Best-fit parameters from WMAP, 2dFGRS and  $\text{Ly}\alpha$  data

Parameter	Value
$A$	$0.83^{+0.09}_{-0.08}$
$n_s$	$0.93 \pm 0.03$
$dn_s/d\ln k$	$-0.031^{+0.016}_{-0.017}$
$\tau$	$0.17 \pm 0.06$
$h$	$0.71^{+0.04}_{-0.03}$
$\Omega_m h^2$	$0.135^{+0.008}_{-0.009}$
$\Omega_b h^2$	$0.0224 \pm 0.0009$

The situation is expected to improve as long as WMAP will collect data for a total of 4 years of operations. This will increase the signal-to-noise ratio by a factor of 2 with respect to 1 year data yielding better estimation of cosmological parameters. Although the picture is clear in its main features it is not complete yet. There are indeed some open issues raised by the WMAP data: as usual a new powerful experiment will answer to many questions but it will also invariably open many new ones. There is, for example, the issue of low level of quadrupole and the “strange” alignment of quadrupole and octupole [194] for which an explanation is not at hand. It is possible that these low multipoles are still affected by not-subtracted foreground emissions for which WMAP is not optimally designed.

These questions will be possibly answered by a real full-sky imaging experiment with the capability of detecting CMB anisotropy up to the maximum relevant multipole corresponding to the physical dimension of the Last Scattering Surface, which is the goal of the ESA Planck mission. The high quality of Planck data is expected to reduce the error bars in cosmological parameters at the level of few percent thanks to the combination of temperature and polarisation data, and for a wide set of cosmological parameters [195] the final accuracy will be largely independent from auxiliary informations coming from other classes of astronomical observations.

What do we expect after Planck? Recently it has become clear the the future of CMB experiments is in the imaging of the polarisation anisotropy. We are in the same situation

as we were before COBE-DMR with respect temperature anisotropy detection. Polarisation is a powerful tool probing directly the Last Scattering Surface, in particular the detection of *B*-modes is a key issue since it will strongly constrain the picture of our Universe.

## 6 FUTURE CHALLENGES

In analogy with what happened after FIRAS measurement of the frequency spectrum [196], after Planck one might expect a decrease of activity in traditional anisotropy projects. However, in some areas Planck will act as a pioneering mission rather than as a conclusive one. Two main research directions can be anticipated: precision measurements of CMB polarisation and deep imaging at sub-arcminute scales. On these objectives, a number of sub-orbital programs are ongoing or are being planned for the coming several years.

### 6.1 Polarisation

Though extraordinary, the cosmological information obtainable with temperature anisotropy alone is far less than what in principle can be achieved with high-precision CMB polarimetry. Linear polarisation in the CMB arises from Thomson scattering of anisotropic radiation at last scattering [197], and it encodes information complementary to temperature anisotropies.

Even the remarkable sensitivity of Planck to *Q* and *U* Stokes parameters will be far from fully extracting the information encoded in the cosmic polarised signal. In particular higher sensitivity will be needed to measure in detail the B-mode spectrum, related to gravitational effects. Deep polarisation maps may give indications on the inflation energy scale, thus probing ultra-high energy physics to levels beyond what can be obtained with any conceivable terrestrial particle accelerator. Even more subtle, but not less interesting, will be the exploration of effects of weak gravitational lensing through the distortion of the CMB polarisation on small scales [198].

Until recently, only upper limits to CMB polarisation existed (see [199] and references therein) at a level 10–15  $\mu\text{K}$ . A major recent breakthrough has been the detection of E-mode polarisation by the ground-based interferometry experiment DASI [155] at few  $\mu\text{K}$  level, and the detection by both WMAP and DASI of the T-E correlation [24, 155]. The full-sky data of WMAP allow to trace the correlation up to the largest scales, while DASI is limited by sample variance. The T-E correlation is a consequence of the fact that the fluid velocities which lead to polarisation are produced by the same density perturbations which are responsible for temperature anisotropy. These results provide confirmation of the standard model and, as discussed in Sect. 5.3.2, the T-E correlation on large angular scales observed by WMAP gives evidence of reionisation at redshifts  $11 < z < 30$ .

At the same time, these first polarisation detections open up a new stage in CMB research. Both DASI and WMAP are still ongoing, and a number of new CMB polarisation experiments are being prepared from ground, balloon and eventually space.

### 6.1.1 Ongoing and planned Polarisation experiments

A few ground-based polarisation instruments are currently taking data (see e.g. [200]). The CBI is operative at the Atacama plateau in Chile [201] and it is based on Ka-band low-noise HEMT amplifiers. CBI achieves a sensitivity similar to that of DASI, but it improves the angular resolution by a factor  $\sim 3$ . The CAPMAP [202] was operated in 2003 with four W-band correlation receivers coupled to the Bell Labs 7-meter telescope leading to  $\sim 5'$  resolution. In the future, 16 radiometers in W band and four in Q band are foreseen. The Beast instrument [203], currently taking data from the White Mountain Research Station, is planned to be converted into a W-band polarimeter. In addition, two new PSB bolometric arrays are being developed, both expected for 2005: BICEP (Back-ground Imaging of Cosmic Extragalactic Polarisation), to be operated from the South Pole [204], and QUEST (Q and U Extra-galactic Survey Telescope) to be coupled to the DASI telescope. BICEP will be sensitive to scales  $10 < \ell < 200$  and QUEST in the overlapping range  $100 < \ell < 2000$ , both with sensitivity adequate to mapping the E-mode angular power spectrum, and possibly detection of B-modes.

Ongoing balloon-borne polarisation programs include Boomerang [205] which made an Antarctic 12-day LDB flight in January 2003, and MAXIPOL which had a successful flight in May 2003 from Fort Sumner, New Mexico. The focal plane of Boomerang was reconfigured for its 2003 flight with PSBs developed at JPL, similar to those foreseen for Planck HFI. The MAXIPOL polarimeter was obtained as a refurbishment of MAXIMA by adding a rotating half-wave plate and fixed polarizing grids in front of the horns. Both Boomerang and MAXIPOL have the sensitivity to detect E-mode polarisation at degree scales. A space experiment to search for polarisation at  $> 7^\circ$  scales is SPORt (Sky Polarisation Observatory) [206] proposed for implementation on the International Space Station. The instrument is based on HEMT radiometers cooled at  $\sim 90$  K and operating at 4 frequencies in the 20–90 GHz range. The balloon-borne counterpart of SPORt, called BaR-SPORt (Balloon-borne Radiometers for Sky Polarisation) [207] has a multi-feed focal plane of polarimeters in W band at the focus of an on-axis telescope reaching sub-degree angular resolution.

After its first detection, rapid progress can be expected in the observation of the E-mode power spectrum. All these measurements are extremely demanding in terms of control of instrumental systematic errors and foreground contamination. The challenge will be to obtain results which are actually limited by the extraordinary sensitivity of the cryogenically cooled detectors. The present generation of instruments will measure CMB polarisation with previously unreachable sensitivity, and will also explore new techniques and detectors, possibly uncovering unexpected challenges in terms of instrumental and astrophysical limitations.

### 6.1.2 Polarisation: the future

The polarisation amplitude, now known to be at few  $\mu\text{K}$  level, imposes new requirements on instrument sensitivity. Advances in both bolometer and coherent receiver technology are promising, particularly in the direction of large optimised focal plane arrays. Compact and relatively low cost correlation receivers may be produced in the near future based on integrated circuit technologies. Arrays of hundreds of radiometers may be assembled either as independent ra-

diometer channels or as future interferometers. Similarly, large arrays for bolometers are being experimented (see, e.g., [208]) based on monolithic arrays developed at Caltech/JPL. Arrays of  $\sim 1000$  or more channels are possible with this technology. An example is the planned experiment Polarbear, a 3 meter off-axis telescope dedicated to CMB polarisation measurements with as many as 1000–3000 elements of polarisation-sensitive antenna-coupled bolometers.

Multi-frequency observations, possibly with matching beam sizes, would be needed to tackle the subtle problem of polarised foreground separation. It is difficult to anticipate which systematic effects could represent limiting factors at sub- $\mu\text{K}$  levels; it is likely that thermal stability at the cryogenic temperatures needed by the ultra-high sensitivity detectors (either radiometers or bolometers) will be a major challenge; also, a multi-channel off-axis instrument, pushed at extreme sensitivities, would place critical requirements for ultra-low cross-polarisation.

The sensitivity requirements for a full-sky, high-precision polarisation survey are extremely demanding. The expected B-mode amplitude induced by gravitational waves is  $\sim 0.1\%$  to  $1\%$  of temperature  $\Delta T/T$ : a high signal-to-noise imaging requires a noise per pixel  $\sim 0.05 \mu\text{K}$ , i.e. about 300 times better than Planck. This is beyond the foreseeable future, but an intermediate step aiming at a full measurement of the power spectra, with sensitivity  $0.5 \mu\text{K}$  per  $10'$  resolution element, can be approached extrapolating existing technology. The growing CMB community is now already in the process of discussing plans for a possible fourth-generation space mission dedicated to CMB polarisation. As in the case of Planck for temperature anisotropy, such mission would be expected to provide polarisation observations limited by cosmic variance and unavoidable foregrounds.

## 6.2 Fine-scale temperature signatures

On angular scales  $\sim 1'$  and below the CMB is highly influenced by interaction with intervening ionised material. The CMB passed through the cosmic “dark ages”, before star and quasar formation, from which direct observation is extremely difficult to obtain. Using the CMB as a high redshift back-light, the study of its arcmin scale features may be one of the most powerful techniques to observe the very early processes of structure formation. Furthermore, accurate S-Z measurements can be made to very high redshifts [209], all the way back to the cluster formation era [210]. Planck angular resolution is not sufficient to fully cover this promising area of CMB studies. The S-Z effect from clusters is by far the dominant secondary source. Once this will be well identified and mapped, sky regions free from S-Z and other local foregrounds could be searched at  $\sim 1'$  scales for fainter secondary signatures, such as those from gravitational collapse of large scale ( $\sim 100 \text{ Mpc}$ ) structures, bulk motion of plasma (the “Ostriker-Vishniac effect”), effects of the evolution of gravitational potentials on CMB photons (the “integrated Sachs-Wolfe effect” and the “Rees-Sciama effect”), lensing-induced signatures from clusters [211], signature of local ionisation events [212], and details of the ionisation history of the Universe.

It is easy to expect that the WMAP and the future Planck surveys will trigger observations in selected sky areas searching for detailed, physically interesting features. New instruments and observing strategies will be, and are already being, developed for the purpose.

### 6.2.1 Ongoing and planned fine-scale observations

The brightest clusters give a S-Z thermal component  $\sim 1$  mK, while the kinetic effects is expected to be  $\sim 10$  times lower. Signatures such as filaments from in-falling clusters are expected at  $\sim 10$   $\mu$ K level. Current bolometric or HEMT-based instruments, either filled aperture arrays or interferometers, are able to approach sub- $\mu$ K sensitivity in very localised areas.

Most ground based projects currently active or planned are based on interferometer instruments, capable of very high angular resolution. As an example, the interferometer experiment called AMiBA (Array for Microwave Background Anisotropy), is expected to be soon operative [213]. The instrument is being built for fine-scale CMB temperature imaging, for measurements of the polarisation anisotropy, as well as for observations of the Sunyaev-Zel'dovich Effect. This will be a 19 elements, W-band array by the Academia Sinica, Institute of Astronomy and Astrophysics, and National University of Taiwan. Two sets of array dishes are planned, with 1.2 meter and 0.3 meter size. Initial observations are planned to start in 2004.

Antarctic winter fine-scale observations may also have a long future. The Arcminute Cosmology Bolometer Array Receiver (ACBAR) is a 16 element array of bolometers cooled at 0.23 K designed for observation of small scale anisotropy and Sunyaev-Zel'dovich effect. The experiment, run by the Centre for Astrophysical Research in Antarctica (CARA), was deployed at the South Pole in December 2000. Preliminary results in the range  $200 < \ell < 2200$  based on data taken in the austral winter of 2001 were presented [157] including serendipitous discoveries of high redshift clusters via their S-Z effect.

### 6.2.2 Fine-scale: the future

At wavelengths  $\lambda \approx 1$  mm, a  $\lesssim 1'$  resolution translates in a telescope aperture typically  $D \sim 10$  m. New telescopes, to be coupled with ultra-high sensitivity arrays, are required to ensure sub-arcmin resolutions. Some of these are already in an advanced stage of planning. The South Pole Telescope (SPT) is an off-axis precision telescope with an aperture of 8 meters. The SPT is expected to be installed at the South Pole site in 2006, together with a large 1000-element bolometric radiometer, and possibly with a large focal plane polarimeter. Another planned high-resolution millimetre telescope is the Atacama Cosmology Telescope (ACT), a 6-meter off-axis to be deployed in Chile.

Although not primarily designed for CMB studies, the extraordinary resolution and sensitivity at  $\nu \lesssim 20$  GHz of the Square Kilometre Array (SKA)<sup>6</sup> will allow an extremely accurate control of radio source fluctuations at very large multipoles useful for precise re-analysis of CMB dedicated surveys and will represent at the same time a good opportunity for studying CMB secondary anisotropies relevant at multipoles  $\approx 104 - 105$  (e.g. induced by thermal SZ, Ostriker-Vishniac and Rees-Sciama effects), and to detect and map thermal SZ effects at sub-arcmin scales associated to gas heated at its virial temperature in proto-galaxies or to strong energy injections from quasars [214].

Focal plane arrays for deep arcmin imaging are likely to be simultaneously sensitive to linear

---

<sup>6</sup>[http://www.skatelescope.org/ska\\_concept.shtml](http://www.skatelescope.org/ska_concept.shtml)

polarisation. As mentioned, polarisation-sensitive arrays with up to 1000 elements or more are being envisioned. In the future, high precision fine-scale CMB imaging would call for very wide frequency coverage, with ancillary monitoring at low frequency ( $< 5$  GHz) and high frequency ( $> 5$  THz) to safely remove unrelated foregrounds as well as backgrounds (such as primary CMB anisotropy, regarded as a source of confusion in this context).

These observations can be expected to progress for several years with ground-based instrumentation. A future sky survey of clusters velocities based on their S-Z features throughout the entire Hubble volume could, in principle, map the evolution of velocity fields over much of the history of the Universe. Eventually, a fine-scale, full-sky survey will only be possible with a space programme, currently out of reach.

## 7 CONCLUSIONS

After the discovery of CMB temperature anisotropies by COBE, a great experimental effort has been accomplished with ground-based and balloon-borne experiments and recently by the WMAP space mission, leading to a good determination of the angular power spectrum up to sub-degree scales. The acoustic nature of the spectrum, expected by theory, is now beautifully matched by observation. This is a truly remarkable achievement. The recent detection of polarisation E-modes and the TE correlation represents a further striking confirmation of the soundness of standard cosmology and provides new incentive to the experimental growth of CMB research. However, these rewarding results are probably only a foretaste of the precision observation attainable by the forthcoming generations of experiments, culminating with the Planck mission. The Planck survey will generate an unprecedented set of multi-frequency temperature and polarisation data, leading to major improvement in the determination of cosmological parameters and to a new profound verification of our cosmological understanding.

Beyond Planck, it is likely that CMB observations will concentrate on precision polarisation measurements (especially searching for gravitational wave signatures in the B-mode spectrum) and deep sub-arcmin imaging of secondary anisotropies. Large arrays of cryogenic detectors, now under study, should be capable of reaching the extreme instrument sensitivity required. However, this will not be enough. The experience of the past decades has shown that CMB measurements are typically limited by systematic effects, either of instrumental or astronomical nature, some of which have been discussed in this review. These limitations will need to be explored at a much deeper level in future high-precision enterprises.

Precision measurements of the CMB are able to shed light on very high energy phenomena occurring in the primordial cosmic environment, as well as on the physical history of the Universe. Today, observations of the CMB promise to remain one of the most powerful cosmological probes for yet many years in the future.

## Acknowledgements

The completion of this review has been greatly helped, either directly or indirectly, by the work of many people, in particular by the Planck Science Team, by the Planck-LFI consortium and by the Boomerang and MAXIMA teams. We would also like to thank the WMAP science

team for figure permission and L.A. Popa, D. Sáez, L. Toffolatti, L. Danese and G. De Zotti for useful discussions.

## References

- [1] Penzias, A. A. and Wilson, R. W., 1965, *ApJ*, 142, 419–421.
- [2] Reber, G., 1940, *ApJ*, 91, 621–624.
- [3] Reber, G., 1944, *ApJ*, 100, 279.
- [4] Hubble, E., 1929, *Proceedings of the National Academy of Science*, 15, 168–173.
- [5] Gamow, G., 1946, *Physical Review*, 70, 572–573.
- [6] Fixsen, D. J., Cheng, E. S., Gales, J. M., et al., 1996, *ApJ*, 473, 576.
- [7] Bersanelli, M., Bensadoun, M., de Amici, G., et al., 1994, *ApJ*, 424, 517–529.
- [8] de Amici, G., Limon, M., Smoot, G. F., et al., 1991, *ApJ*, 381, 341–347.
- [9] Bensadoun, M., Bersanelli, M., de Amici, G., et al., 1993, *ApJ*, 409, 1–13.
- [10] Smoot, G. F., Bensadoun, M., Bersanelli, M., et al., 1987, *ApJL*, 317, L45–L49.
- [11] Sironi, G., Bonelli, G., and Limon, M., 1991, *ApJ*, 378, 550–556.
- [12] Salvaterra, R. and Burigana, C., 2002, *MNRAS*, 336, 592–610.
- [13] Smoot, G. F., Bennett, C. L., Kogut, A., et al., 1992, *ApJL*, 396, L1–L5.
- [14] Bersanelli, M., Maino, D., and Mennella, A., 2002, *Riv. Nuovo Cimento*, 25(9).
- [15] R.K., S. and A.M., W., 1967, *Astrophysical Journal*, 147, 73.
- [16] Silk, J., 1968, *ApJ*, 151, 459.
- [17] Bond, J. R., Jaffe, A. H., and Knox, L., 2000, *ApJ*, 533, 19–37.
- [18] Verde, L., Peiris, H. V., Spergel, D. N., et al., 2003, *ApJS*, 148, 195–211.
- [19] Madau, P., 2003, *IAU Symposium*, 687.
- [20] Becker, R. H., Fan, X., White, R. L., et al., 2001, *AJ*, 122, 2850–2857.
- [21] Sugiyama, N., Silk, J., and Vittorio, N., 1993, *ApJL*, 419, L1.
- [22] de Bernardis, P., Balbi, A., de Gasperis, G., Melchiorri, A., and Vittorio, N., 1997, *ApJ*, 480, 1.
- [23] Hu, W., 2000, *ApJ*, 529, 12–25.

- [24] Kogut, A., Spergel, D. N., Barnes, C., et al., 2003, *ApJS*, 148, 161–173.
- [25] Spergel, D. N., Verde, L., Peiris, H. V., et al., 2003, *ApJS*, 148, 175–194.
- [26] Valageas, P., Balbi, A., and Silk, J., 2001, *A&A*, 367, 1–17.
- [27] Sunyaev, R. A. and Zeldovich, Y. B., 1972, *Comments on Astrophysics*, 4, 173.
- [28] Komatsu, E. and Seljak, U., 2002, *MNRAS*, 336, 1256–1270.
- [29] Blanchard, A. and Schneider, J., 1987, *A&A*, 184, 1–2.
- [30] Seljak, U., 1996, *ApJ*, 463, 1.
- [31] Kallosh, R. and Linde, A., 1997, *Phys. Rev. D*, 56, 3509–3514.
- [32] Contaldi, C. R., Bean, R., and Magueijo, J., 1999, *Physics Letters B*, 468, 189–194.
- [33] Martin, J., Riazuelo, A., and Sakellariadou, M., 2000, *Phys. Rev. D*, 61, 83518.
- [34] Bartolo, N., Matarrese, S., and Riotto, A., 2002, *Phys. Rev. D*, 65, 103505.
- [35] Gangui, A., Martin, J., and Sakellariadou, M., 2002, *Phys. Rev. D*, 66, 83502.
- [36] Gupta, S., Berera, A., Heavens, A. F., and Matarrese, S., 2002, *Phys. Rev. D*, 66, 43510.
- [37] Liguori, M., Matarrese, S., and Moscardini, L., 2003, Submitted to *ApJ*, astro-ph/0306248.
- [38] Bartolo, N., Matarrese, S., and Riotto, A., 2003, *ArXiv Astrophysics e-prints*, astro-ph/0309692.
- [39] Gangui, A., Pogosian, L., and Winitzki, S., 2001, *Phys. Rev. D*, 64, 43001.
- [40] Levin, J., 2002, *Phys. Rep.*, 365, 251–333.
- [41] Eriksen, H. K., Banday, A. J., and Górski, K. M., 2002, *A&A*, 395, 409–415.
- [42] Gott, J. R. I., Park, C., Juskiewicz, R., et al., 1990, *ApJ*, 352, 1–14.
- [43] Schmalzing, J. and Gorski, K. M., 1998, *MNRAS*, 297, 355–365.
- [44] Novikov, D., Schmalzing, J., and Mukhanov, V. F., 2000, *A&A*, 364, 17–25.
- [45] Heavens, A. F. and Gupta, S., 2001, *MNRAS*, 324, 960–968.
- [46] Doré, O., Colombi, S., and Bouchet, F. R., 2003, *MNRAS*, 344, 905–916.
- [47] Barreiro, R. B., Martínez-González, E., and Sanz, J. L., 2001, *MNRAS*, 322, 411–418.
- [48] Phillips, N. G. and Kogut, A., 2001, *ApJ*, 548, 540–549.
- [49] Winitzki, S. and Wu, J. H. P., *ArXiv Astrophysics e-prints*, astro-ph/0007213.

- [50] Hu, W., 2001, *Phys. Rev. D*, 64, 83005.
- [51] Kunz, M., Banday, A. J., Castro, P. G., Ferreira, P. G., and Górski, K. M., 2001, *ApJL*, 563, L99–L102.
- [52] Komatsu, E. and Spergel, D. N., 2001, *Phys. Rev. D*, 63, 63002.
- [53] Komatsu, E., Wandelt, B. D., Spergel, D. N., Banday, A. J., and Górski, K. M., 2002, *ApJ*, 566, 19–29.
- [54] De Troia, G., Ade, P. A. R., Bock, J. J., et al., 2003, *MNRAS*, 343, 284–292.
- [55] Chiang, L.-Y., Christensen, P. R., Jörgensen, H. E., et al., 2002, *A&A*, 392, 369–376.
- [56] Marinucci, D. and Piccioni, M., 2002, *Annals of Statistics*, in press.
- [57] Hansen, F. K., Marinucci, D., Natoli, P., and Vittorio, N., 2002, *Phys. Rev. D*, 66, 63006.
- [58] Hansen, F. K., Marinucci, D., and Vittorio, N., 2003, *Phys. Rev. D*, 67, 123004.
- [59] Barreiro, R. B. and Hobson, M. P., 2001, *MNRAS*, 327, 813–828.
- [60] Barreiro, R. B., Hobson, M. P., Lasenby, A. N., et al., 2000, *MNRAS*, 318, 475–481.
- [61] Gonzalez, E. M., Gallegos, J. E., Argueso, F., Cayon, L., and Sanz, J. L., 2002, *MNRAS*, 336, 22.
- [62] Mukherjee, P., Hobson, M. P., and Lasenby, A. N., 2000, *MNRAS*, 318, 1157–1163.
- [63] Ferreira, P. G., Magueijo, J., and Gorski, K. M., 1998, *ApJL*, 503, L1.
- [64] Banday, A. J., Zaroubi, S., and Górski, K. M., 2000, *ApJ*, 533, 575–587.
- [65] Komatsu, E., Kogut, A., Nolte, M. R., et al., 2003, *ApJS*, 148, 119–134.
- [66] Chiang, L., Naselsky, P. D., Verkhodanov, O. V., and Way, M. J., 2003, *ApJL*, 590, L65–L68.
- [67] Naselsky, P. D., Verkhodanov, O. V., Chiang, L., and Novikov, I. D., 2003, Submitted to *ApJ*, astro-ph/0300235.
- [68] Coles, P., Dineen, P., Earl, J., and Wright, D., 2003, Submitted to *MNRAS*, astro-ph/0300252.
- [69] Park, C., 2003, Submitted to *MNRAS*, astro-ph/0307469.
- [70] Vielva, P., Martinez-Gonzalez, E., Barreiro, R. B., Sanz, J. L., and Cayon, L., 2003, *ArXiv Astrophysics e-prints*, astro-ph/0300273.
- [71] Smoot, G. F., 1999, *ASP Conf. Ser.* 181: *Microwave Foregrounds*, 61.

- [72] Haslam, C. G. T., Stoffel, H., Salter, C. J., and Wilson, W. E., 1982, *A&A S*, 47, 1.
- [73] Reich, P. and Reich, W., 1986, *A&A S*, 63, 205–288.
- [74] Jonas, J. L., Baart, E. E., and Nicolson, G. D., 1998, *MNRAS*, 297, 977–989.
- [75] Platania, P., Burigana, C., Maino, D., et al., 2003, Accepted for publication in *A&A*, astro-ph/0303031.
- [76] Bennett, C. L., Halpern, M., Hinshaw, G., et al., 2003, *ApJS*, 148, 1–27.
- [77] Tegmark, M. and Efstathiou, G., 1996, *MNRAS*, 281, 1297–1314.
- [78] Lasenby, A. N., 1997, *Microwave Background Anistropies*, 453.
- [79] Baccigalupi, C., Burigana, C., Perrotta, F., et al., 2001, *A&A*, 372, 8–21.
- [80] Baccigalupi, C., Perrotta, F., De Zotti, G., et al., 2003, Accepted for publication in *MNRAS*.
- [81] Paladini, R., Burigana, C., Davies, R. D., et al., 2003, *A&A*, 397, 213–226.
- [82] Paladini, R., DeZotti, G., and Davies, R. D., 2003, Submitted to *MNRAS*, astro-ph/0309350.
- [83] Finkbeiner, D. P., 2003, *ApJS*, 146, 407–415.
- [84] Dickinson, C., Davies, R. D., and Davis, R. J., 2003, *MNRAS*, 341, 369–384.
- [85] Kogut, A., Banday, A. J., Bennett, C. L., et al., 1996, *ApJ*, 460, 1.
- [86] Schlegel, D. J., Finkbeiner, D. P., and Davis, M., 1998, *ApJ*, 500, 525.
- [87] Banday, A. J., Dickinson, C., Davies, R. D., Davis, R. J., and Gorski, K. M., 2003, Accepted for publication in *MNRAS*, astro-ph/0302181.
- [88] Maino, D., Banday, A. J., Baccigalupi, C., Perrotta, F., and Gorski, K. M., 2003, *MNRAS*, 344, 544.
- [89] de Oliveira-Costa, A., Kogut, A., Devlin, M. J., et al., 1997, *ApJL*, 482, L17.
- [90] Leitch, E. M., Readhead, A. C. S., Pearson, T. J., and Myers, S. T., 1997, *ApJL*, 486, L23.
- [91] Draine, B. T. and Lazarian, A., 1998, *ApJL*, 494, L19.
- [92] Franceschini, A., Toffolatti, L., Danese, L., and De Zotti, G., 1989, *ApJ*, 344, 35–45.
- [93] Toffolatti, L., Argueso Gomez, F., De Zotti, G., et al., 1998, *MNRAS*, 297, 117–127.

- [94] De Zotti, G., Toffolatti, L., Argüeso, F., et al., 1999, AIP Conf. Proc. 476: 3K cosmology, 204.
- [95] Mennella, A., Bersanelli, M., Seiffert, M., et al., 2003, A&A, 410, 1089–1100.
- [96] Bersanelli, M., Mattaini, E., Santambrogio, E., et al., 1998, Experimental Astronomy, 8, 231–238.
- [97] Barnes, C., Limon, M., Page, L., et al., 2002, ApJ Suppl. Series, 143, 567–576.
- [98] Murphy, J. A., Colgan, R., Gleeson, E., et al., 2002, AIP Conf. Proc. 616: Experimental Cosmology at Millimetre Wavelengths, 282–289.
- [99] Villa, F., Sandri, M., Mandolesi, N., et al., 2003, Experimental Astronomy, in press.
- [100] Welford, W. T. and Winston, R., 1978, The optics of nonimaging concentrators - Light and solar energy, New York: Academic Press, 1978.
- [101] Burigana, C., Maino, D., Mandolesi, N., et al., 1998, A&A S, 130, 551–560.
- [102] Fosalba, P., Doré, O., and Bouchet, F. R., 2002, Physical Review D, 65, 63003.
- [103] Mandolesi, N., Bersanelli, M., Burigana, C., et al., 2000, A& A Suppl., 145, 323–340.
- [104] Page, L., Barnes, C., Hinshaw, G., et al., 2003, Apj Suppl. Series, 148, 39–50.
- [105] Arnau, J. V. and Sáez, D., 2000, New Astronomy, 5, 121–135.
- [106] Burigana, C. and Sáez, D., 2003, A&A, 409, 423–437.
- [107] Dubruel, D., Fargan, G., Cornut, M., et al., 2000, ESA Conf. Proc. SP444: AP2000 Millennium Conference on Antennas & Propagation.
- [108] Villa, F., Bersanelli, M., Burigana, C., et al., 2002, AIP Conf. Proc. 616: Experimental Cosmology at Millimetre Wavelengths, 224–228.
- [109] Page, L., Jackson, C., Barnes, C., et al., 2003, ApJ, 585, 566–586.
- [110] Sandri, F., Bersanelli, M., Burigana, C., et al., 2003, ESA Conf. Proc. WPP-212: 3rd ESA Workshop on Millimeter Wave Technology and Applications, 199.
- [111] Sandri, M., Villa, F., Nesti, R., et al., 2003, Submitted to A& A, astro-ph/0305152, also in astro-ph/0305152.
- [112] Burigana, C., Sandri, M., Villa, F., et al., 2003, Submitted to A& A, astro-ph/0303645, also in astro-ph/0303645.
- [113] van der Ziel, A., 1976, Noise in Measurements, New York: John Wiley and Sons, 1976.
- [114] Einstein, A., 1906, Ann. Phys, 19, 289.

- [115] Johnson, J. B., 1928, *Physical Review*, 32, 97–109.
- [116] Nyquist, H., 1928, *Physical Review*, 32, 110–113.
- [117] Schottky, W., 1918, *Ann. Phys*, 57, 541.
- [118] Wong, H., 2003, *Microelectron. Reliab.*, 43, 585–599.
- [119] Smoot, G., Bennett, C., Weber, R., et al., 1990, *ApJ*, 360, 685–695.
- [120] Jarosik, N., Bennett, C. L., Halpern, M., et al., 2003, *ApJS*, 145, 413–436.
- [121] Seiffert, M., Mennella, A., Burigana, C., et al., 2002, *A&A*, 391, 1185–1197.
- [122] Maris, M., Maino, D., Burigana, C., and Pasian, F., 2000, *A&A S*, 147, 51–74.
- [123] Maris, M., Maino, D., Burigana, C., et al., 2003, Accepted for publication in *A&A*, astro-ph/0304089.
- [124] Maino, D., Burigana, C., and Pasian, F., 2003, *New Astronomy*, 8, 711–718.
- [125] Lineweaver, C. H., Smoot, G. F., Bennett, C. L., et al., 1994, *ApJ*, 436, 452–455.
- [126] Wright, E. L., Hinshaw, G., and Bennett, C. L., 1996, *ApJL*, 458, L53–L55.
- [127] Hinshaw, G., Barnes, C., Bennett, C. L., et al., 2003, *ApJS*, 148, 63–95.
- [128] Tegmark, M., 1997, *ApJL*, 480, L87.
- [129] Natoli, P., de Gasperis, G., Gheller, C., and Vittorio, N., 2001, *A&A*, 372, 346–356.
- [130] Doré, O., Teyssier, R., Bouchet, F. R., Vibert, D., and Prunet, S., 2001, *A&A*, 374, 358–370.
- [131] Maino, D., Burigana, C., Górski, K. M., Mandolesi, N., and Bersanelli, M., 2002, *A&A*, 387, 356–365.
- [132] C. Burigana, C., Natoli, P., Vittorio, N., Mandolesi, N., and Bersanelli, M., 2001, *Experimental Astronomy*, 12, 87–106.
- [133] Terenzi, L., Bersanelli, M., Burigana, C., et al., 2002, *AIP Conf. Proc.* 616: *Experimental Cosmology at Millimetre Wavelengths*, 245–247.
- [134] Cappellini, P., Maino, D., Albetti, G., et al., 2003, *A&A*, 409, 375–385.
- [135] Maris, M., Burigana, C., Cremonese, G., Marzari, F., and Fogliani, S., 2003, to be published in *Proc. of the 5th Italian Conference of Planetary Sciences*, Gallipoli, Lecce, Italy, September 15–19.
- [136] Maris, M., Burigana, C., Cremonese, G., et al., 2003, to be published in *Proc. XLVII National Conference of the Italian Astronomical Society*, Trieste, Italy, April 14–17.

- [137] Kogut, A., Banday, A. J., Bennett, C. L., et al., 1996, *ApJ*, 470, 653.
- [138] Gorski, K. M., Banday, A. J., Bennett, C. L., et al., 1996, *ApJL*, 464, L11.
- [139] Hinshaw, G., Banday, A. J., Bennett, C. L., et al., 1996, *ApJL*, 464, L25.
- [140] Romeo, G., Ali, S., Femenía, B., et al., 2001, *ApJL*, 548, L1–L4.
- [141] Davies, R. D., Watson, R. A., and Gutierrez, C. M., 1996, *MNRAS*, 278, 925–939.
- [142] Dicker, S. R., Melhuish, S. J., Davies, R. D., et al., 1999, *MNRAS*, 309, 750–760.
- [143] Gundersen, J. O., Lim, M., Staren, J., et al., 1995, *ApJL*, 443, L57–L60.
- [144] Platt, S. R., Kovac, J., Dragovan, M., Peterson, J. B., and Ruhl, J. E., 1997, *ApJL*, 475, L1.
- [145] Coble, K., Dragovan, M., Kovac, J., et al., 1999, *ApJL*, 519, L5–L8.
- [146] Peterson, J. B., Griffin, G. S., Newcomb, M. G., et al., 2000, *ApJL*, 532, L83–L86.
- [147] Wollack, E. J., Devlin, M. J., Jarosik, N., et al., 1997, *ApJ*, 476, 440.
- [148] Devlin, M. J., de Oliveira-Costa, A., Herbig, T., et al., 1998, *ApJL*, 509, L69–L72.
- [149] Leitch, E. M., Readhead, A. C. S., Pearson, T. J., et al., 2000, *ApJ*, 532, 37–56.
- [150] Baker, J. C., Grainge, K., Hobson, M. P., et al., 1999, *MNRAS*, 308, 1173–1178.
- [151] Partridge, R. B., Richards, E. A., Fomalont, E. B., Kellermann, K. I., and Windhorst, R. A., 1997, *ApJ*, 483, 38.
- [152] Subrahmanyam, R., Kesteven, M. J., Ekers, R. D., Sinclair, M., and Silk, J., 1998, *MNRAS*, 298, 1189–1197.
- [153] Holzapfel, W. L., Wilbanks, T. M., Ade, P. A. R., et al., 1997, *ApJ*, 479, 17.
- [154] Halverson, N. W., Leitch, E. M., Pryke, C., et al., 2002, *ApJ*, 568, 38–45.
- [155] Kovac, J. M., Leitch, E. M., Pryke, C., et al., 2002, *Nature*, 420, 772–787.
- [156] Pearson, T. J., Mason, B. S., Readhead, A. C. S., et al., 2003, *ApJ*, 591, 556–574.
- [157] Kuo, C. L., Ade, P. A. R., Bock, J. J., et al., 2002, Submitted to *ApJ*, astro-ph/0202289.
- [158] Meyer, S. S., Cheng, E. S., and Page, L. A., 1991, *ApJL*, 371, L7–L9.
- [159] de Bernardis, P., de Gasperis, G., Masi, S., and Vittorio, N., 1994, *ApJL*, 433, L1–L4.
- [160] Tucker, G. S., Gush, H. P., Halpern, M., and Towlson, W., 1997, *Microwave Background Anisotropies*, 167.

- [161] Tanaka, S. T., Clapp, A. C., Devlin, M. J., et al., 1996, *ApJL*, 468, L81.
- [162] de Bernardis, P., Ade, P. A. R., Bock, J. J., et al., 2000, *Nature*, 404, 955–959.
- [163] Netterfield, C. B., Ade, P. A. R., Bock, J. J., et al., 2002, *ApJ*, 571, 604–614.
- [164] Hanany, S., Ade, P., Balbi, A., et al., 2000, *ApJL*, 545, L5–L9.
- [165] Balbi, A., Ade, P., Bock, J., et al., 2000, *ApJL*, 545, L1–L4.
- [166] Benoît, A., Ade, P., Amblard, A., et al., 2003, *A&A*, 399, L19–L23.
- [167] Bennett, C. L., Bay, M., Halpern, M., et al., 2003, *ApJ*, 583, 1–23.
- [168] Gorski, K., Hivon, E., and Wandelt, B., 1998, MPA/ESO Cosmology Conference ”Evolution of Large-Scale Structure”, eds. A.J. Banday, R.S. Sheth and L. Da Costa, *PrintPartners Ipskamp, NL*, 37–42.
- [169] Bennett, C. L., Hill, R. S., Hinshaw, G., et al., 2003, *ApJS*, 148, 97–117.
- [170] Efstathiou, G., 2003, *MNRAS*, 343, L95–L98.
- [171] Roddis, N., Kettle, D., Winder, F., et al., 2003, 3<sup>rd</sup> ESA Workshop on millimetre wave technology and applications, 81.
- [172] Sjöman, P., Hughes, N., Jukkala, P., et al., 2003, 3<sup>rd</sup> ESA Workshop on millimetre wave technology and applications, 75.
- [173] Lamarre, J.-M., 1997, *Microwave Background Anistropies*, 31.
- [174] Church, S., Philhour, B., Lange, A., et al., 1996, *Proceedings of the 30th ESLAB Symposium “Submillimetre and Far-Infrared Space Instrumentation”*, 77.
- [175] Bock, J., DelCastillo, H., Turner, A., et al., 1996, *Proceedings of the 30th ESLAB Symposium “Submillimetre and Far-Infrared Space Instrumentation”*, 119.
- [176] Lange, A., Church, S., Mauskopf, P., et al., 1996, *Proceedings of the 30th ESLAB Symposium “Submillimetre and Far-Infrared Space Instrumentation”*, 105.
- [177] Kaplan, J. and Delabrouille, J., 2002, *AIP Conf. Proc.* 609: *Astrophysical Polarized Backgrounds*, 209.
- [178] Bard, S., 1984, *J. Spacecraft & Rockets*, 21, 150–155.
- [179] Wade, L., Bhandari, P., Bowman, Jr., R., et al., 2000, vol. 45A, 499–506.
- [180] Prina, M., Bhandari, P., Bowman, R., et al., 2002, *Advances in Cryogenic Engineering*, *AIP Conference Proceeding Series*, New York, vol. 613, 1201–1208.
- [181] Pearson, D., Prina, M., Borders, J., et al., 2003, *Test Performance of a Closed Cycle Continuous Hydrogen Sorption Cryocooler*, *Kluwer Academic/Plenum Publishers*, vol. 12.

- [182] Bowman, Jr., R., Prina, M., Barber, D., et al., 2003, *Evaluation of Hydride Compressor Elements for the Planck Sorption Cooler*, Kluwer Academic/Plenum Publishers, vol. 12.
- [183] Bradshaw, T. and Orłowska, A., 1997, *Proc. 6th European Symposium on Space Environmental Control Systems*, ESA, vol. SP400, 465–470.
- [184] Benoit, A. and Pugeol, S., 1991, *Physica B*, 169, 457–458.
- [185] Benoît et al., A., 1997, *ESA SP-400: Sixth European Symposium on Space Environmental Control Systems*, 497–502.
- [186] Hobson, M. P., Jones, A. W., Lasenby, A. N., and Bouchet, F. R., 1998, *MNRAS*, 300, 1–29.
- [187] Stolyarov, V., Hobson, M. P., Ashdown, M. A. J., and Lasenby, A. N., 2002, *MNRAS*, 336, 97–111.
- [188] Patanchon, G., Snoussi, H., Cardoso, J. F., and Delabrouille, J., 2003, *ArXiv Astrophysics e-prints*, astro-ph/0302078.
- [189] Maino, D., Farusi, A., Baccigalupi, C., et al., 2002, *MNRAS*, 334, 53–68.
- [190] Mason, B. S., Pearson, T. J., Readhead, A. C. S., et al., 2003, *ApJ*, 591, 540–555.
- [191] Percival, W. J., Baugh, C. M., Bland-Hawthorn, J., et al., 2001, *MNRAS*, 327, 1297–1306.
- [192] Croft, R. A. C., Weinberg, D. H., Bolte, M., et al., 2002, *ApJ*, 581, 20–52.
- [193] Gnedin, N. Y. and Hamilton, A. J. S., 2002, *MNRAS*, 334, 107–116.
- [194] de Oliveira-Costa, A., Tegmark, M., Zaldarriaga, M., and Hamilton, A., 2003, *ArXiv Astrophysics e-prints*, astro-ph/0307282.
- [195] Popa, L. A., Burigana, C., and Mandolesi, N., 2001, *ApJ*, 558, 10–22.
- [196] Mather, J. C., 1996, *IAU Symp. 168: Examining the Big Bang and Diffuse Background Radiations*, 419.
- [197] Rees, M. J., 1968, *ApJL*, 153, L1.
- [198] Zaldarriaga, M., 1997, *Phys. Rev. D*, 55, 1822–1829.
- [199] Hedman, M. M., Barkats, D., Gundersen, J. O., Staggs, S. T., and Winstein, B., 2001, *ApJL*, 548, L111–L114.
- [200] Carlstrom, J. E., Kovac, J., Leitch, E. M., and Pryke, C., 2003, To be published in the proceedings of “The Cosmic Microwave Background and its Polarization”, *New Astronomy Reviews*, (eds. S. Hanany and K.A. Olive), astro-ph/0308478.
- [201] Padin, S., Shepherd, M. C., Cartwright, J. K., et al., 2002, *PASP*, 114, 83–97.

- [202] Barkats, D., 2003, To be published in the proceedings of “The Cosmic Microwave Background and its Polarization”, New Astronomy Reviews (eds. S. Hanany and K. A.Olive), astro-ph/0306002.
- [203] Meinhold, P. R., Bersanelli, M., Childers, J., et al., 2003, Submitted to ApJ, astro-ph/0302034.
- [204] Keating, B. G., Ade, P. A. R., Bock, J. J., et al., 2003, Polarimetry in Astronomy. Edited by Silvano Fineschi . Proceedings of the SPIE, Volume 4843, pp. 284-295 (2003)., 284–295.
- [205] Montroy, T., Ade, P. A. R., Balbi, A., et al., 2003, To be published in the proceedings of “The Cosmic Microwave Background and its Polarization”, New Astronomy Reviews, (eds. S. Hanany and K.A. Olive), astro-ph/0305593.
- [206] Cortiglioni, S., Carretti, E., Orsini, M., et al., 2000, AIP Conf. Proc. 504: Space Technology and Applications International Forum, 91.
- [207] Zannoni, M., Baralis, M., Bernardi, G., et al., 2002, Astrophysical Polarized Backgrounds, held 9-12 October, 2001 in Bologna Italy. Edited by Stefano Cecchini, Stefano Cortiglioni, Robert Sault, and Carla Sbarra. AIP Conference Proceedings, Vol. 609. Melville, NY: American Institute of Physics, 115.
- [208] Dowell, C. D., Allen, C. A., Babu, R. S., et al., 2003, Millimeter and Submillimeter Detectors for Astronomy. Edited by Phillips, Thomas G.; Zmuidzinas, Jonas. Proceedings of the SPIE, Volume 4855, pp. 73-87 (2003)., 73–87.
- [209] Stebbins, A., 1997, astro-ph/9709065.
- [210] Aghanim, N., de Luca, A., Bouchet, F. R., Gispert, R., and Puget, J. L., 1997, A&A, 325, 9–18.
- [211] Seljak, U. and Zaldarriaga, M., 2000, ApJ, 538, 57–64.
- [212] Platania, P., Burigana, C., De Zotti, G., Lazzaro, E., and Bersanelli, M., 2002, MNRAS, 337, 242–246.
- [213] Kesteven, M., 2002, Astrophysical Polarized Backgrounds, held 9-12 October, 2001 in Bologna Italy. Edited by Stefano Cecchini, Stefano Cortiglioni, Robert Sault, and Carla Sbarra. AIP Conference Proceedings, Vol. 609. Melville, NY: American Institute of Physics, 2002., p.156, 156.
- [214] De Zotti, G., Burigana, C., Cavaliere, A., et al., 2003, to be published in Proc. of International Symposium Plasmas in the Laboratory and in the Universe: new insights and new challenges, Como, Italy, September 16-19.